DRAFT: September 28, 2004

The Energy Calibration of the USA X-Ray Experiment

Michael T. Wolff[1]

E. O. Hulburt Center for Space Research, Naval Research Laboratory, Washington, DC 20375

and

Pablo M. Saz-Parkinson[2]

Stanford Linear Accelerator Center, Stanford University, 2575 Sand Hill Rd. Menlo Park, CA 94309

Contents

1 The Unconventional Stellar Aspect Experiment **2**

2 Description of the USA Instrument **3**

2.1 USA Proportional Counters . . . 3

2.2 The USA Response Model . . . 7

2.3 USA Energy Gain Relation . . . 8

2.4 Window Transmission For USA . . . 9

2.5 Energy To Create One Electron-Ion Pair . . . 10

2.6 P-10 Gas Interaction Probability . . . 10

2.7 USA Collimator Response . . . 13

2.8 USA Effective area . . . 14

2.9 Argon Escape Peak . . . 14

2.10 USA Energy Resolution . . . 17

2.11 Partial Charge Collection . . . 17

3 The Energy Calibration of USA **18**

3.1 Calibration Sources . . . 18

3.2 On-ground calibration . . . 19

3.2.1 1996 Ground Data . . . 19

[1]E-mail Address: Michael.Wolff@nrl.navy.mil

[2]pablos@SLAC.Stanford.EDU

3.2.2 1997 Ground Data . . . 20
3.2.3 1998 Ground Data . . . 20
3.3 On-Orbit calibration . . . 24
3.4 DIB Mode 2 . . . 24
3.4.1 8 keV Fluorescence Line . . . 24
3.5 DIB Mode 5 . . . 27

4 USA Response Matrices **35**
4.1 USA Response Matrix Generation Programs . . . 35
4.2 USA Data Modes & Response Matrix Files . . . 35
4.3 Fitting the Crab Energy Spectrum . . . 37

5 Conclusions **38**

6 Appendix: The Amplitude of the Argon-Induced Escape Peak **45**

7 Appendix: Space Charge Effects **49**

8 Appendix: Orbital Dependence of the Gain **50**

9 Appendix: Energy-Channel Boundaries **53**

10 Appendix: Codes **57**

1. The Unconventional Stellar Aspect Experiment

The *Unconventional Stellar Aspect* (USA) experiment was launched aboard the *Advanced Research and Global Observation Satellite* (ARGOS) on February 23, 1999 on a Boeing Delta II rocket from Vandenberg Air Force Base. USA was a reflight of two proportional counter X-ray detectors that were used successfully in the NASA Spartan-1 mission (Kowalski et al. 1993). ARGOS/USA was launched into a circular near-polar (98.7° inclination) sun-synchronous orbit at $\sim$ 830 km altitude for a nominal mission duration of 3 years. The spacecraft operated in a 3-axis stabilized mode with the spacecraft Z-axis always pointed toward the center of the Earth, and the X-axis along the direction of the spacecraft velocity vector. USA was mounted on the back of the ARGOS space craft and acquired celestial targets by offset pointing from the known ARGOS attitude. The polar orbit unfortunately placed USA in a high charged particle radiation environment several times per orbit, greatly reducing the observational duty cycle. The USA detector high voltage turned off when going through the Van Allen radiation belts and the South Atlantic Anomaly with the result that the longest USA observations were approximately 23 minutes. A few months after USA was launched, one of the detectors is thought to have been hit by a piece of space debris, puncturing the thin

mylar window and causing the gas to leak rendering that detector module useless. Fortunately, the other detector was unaffected and was able to perform observations for around 18 months. In November 2000 the second detector module was punctured by a piece of space debris and it also failed, ending the observational portion of the USA mission.

2. Description of the USA Instrument

2.1. USA Proportional Counters

Proportional counters are a type of gas-filled detector that have been used in particle physics since the 1940s, though their origin dates back to 1908, when the first wire chamber, the Geiger-Müller counter, was invented. Multiwire proportional counters have been (and still are) used in X-ray astronomy due to their many positive features, such as good time resolution, reasonable spatial resolution, and relatively low cost. One of their less attractive features is their poor energy resolution. Some detectors, such as semiconductor diode detectors, can have energy resolutions as good as $\sim 3\%$ at 6 keV whereas multiwire proportional chambers have relatively poor energy resolution (theoretically limited to ≥ 15 %).

The proportional chamber gets its name from the fact that for a certain range of applied voltages, the final amplitude of the recorded pulse is approximately proportional to the energy of the incoming particle or photon (however, see below). In general, the charge collected by the anode will depend on the magnitude of the electric field (or voltage) applied to the chamber (see the excellent description of proportional counters in Knoll 2000). The applied high voltage in USA is set such that the electrons produced in the first ionization of the gas are imparted with enough energy to ionize the gas again, causing charge multiplication resulting in an electric signal of sufficient amplitude to be measured. This is in the proportional region in Figure 1. Figure 1 summarizes these four regions of operation in a gas-filled detector.

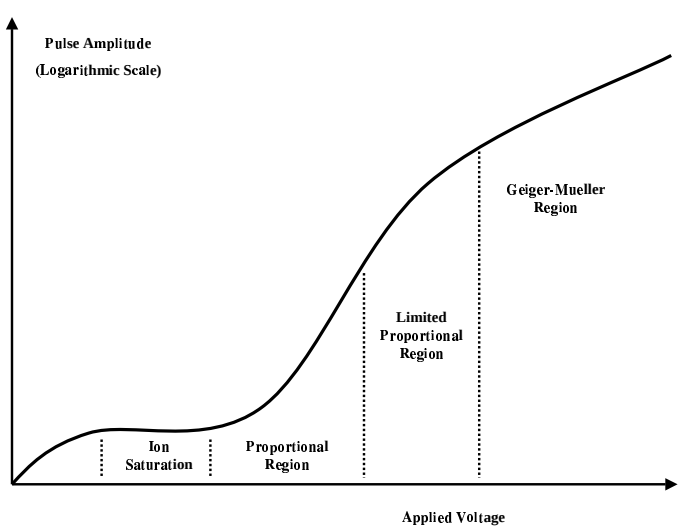

Fig. 1.— The different regions of operation of gas-filled detectors as a function of the applied high voltage. USA operated in the "proportional region".

The choice of gas in a proportional chamber is crucial. Noble gases are normally used because multiplication in these gases takes place at lower electric field strengths than in more complex gases. Noble gases, however, have the drawback that the breakdown region (the limited proportionality region in Figure 1) also occurs at much lower applied voltages. This occurs because as the atoms excited (but not ionized) during the avalanche process return to the ground state, they emit photons at high enough energies to initiate a new avalanches near the cathode. This can also be induced by the neutralization of ions that travel towards the cathode. One way around this problem is to add what is referred to as a "quenching gas," which will absorb these energetic photons before they cause breakdown and then dissipate the excess energy either by inelastic collisions or by dissociation into simpler radicals. The most commonly used gases for this purpose are hydrocarbons, which tend to be efficient at absorbing photons in these energy ranges. The addition of this quenching gas allows multiplication factors as high as 10^5 to 10^6. For a detailed description of the operation of multiwire proportional chambers see Sauli (1977) and Knoll (2000).

In its most basic form, a wire chamber consists of a metallic cylinder containing an ionizing gas and a single anode wire strung along the axis kept at a high voltage. The electric field around the thin anode wire (see Figure 2) is given by Equation 1:

$$E(r) = \frac{V}{r \ln(b/a)} \tag{1}$$

where V is the voltage applied between the anode and cathode, r is the radial distance from the anode wire, a is the anode wire radius and b is the cathode inner radius. As can be seen from Figure 2, the electric field becomes very large as r becomes small. When a photon or particle of sufficient energy interacts with the gas, it ionizes some of the gas atoms and/or molecules, producing ion-electron pairs. The electrons are attracted to the positively charged anode while the ions drift toward the cathode. As the electrons approach the anode wire they are accelerated, and when an electron picks up enough energy, secondary electrons can be produced in collisions with other atoms. For sufficiently high voltage, these will have enough energy to go on to ionize more gas atoms and molecules, and so on, creating an avalanche of electrons in the region surrounding the anode. The electron avalanche becomes significant at about 50 μm from the wire. All the electrons are finally collected at the anode wire, giving rise to an electric pulse.

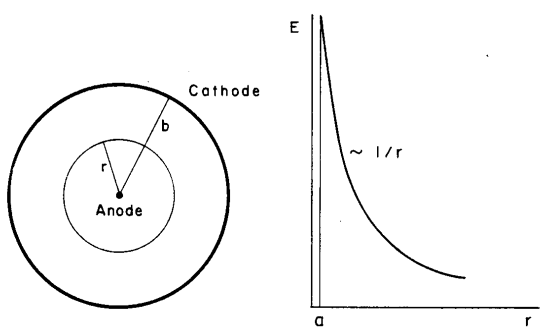

Fig. 2.— The electric field around a thin anode wire (Sauli 1977). The rapid decrease in electric field strength with distance r from the anode wire limits the avalanche region to within a few anode wire radii of its center.

The USA detector onboard the *ARGOS* satellite is a multiwire gas-filled proportional counter which detects X-rays roughly in the 1–15 keV range. The absorption of photons by the detector gas in this energy range produces electron-ion pairs that drift toward the anode (electrons) and the cathode (ions). Charge

multiplication near the anode leads to more pairs which ultimately are absorbed by the anode and cathode resulting in a signal pulse (voltage). An analog-to-digital converter transforms this voltage signal into a *Pulse Height Amplitude* (PHA) channel producing a *count* spectrum. In order to obtain an *energy* spectrum from this count spectrum, we must first understand the instrument response as a function of energy. That is, we must understand the path that a photon emitted at an astrophysical source will take to be recorded in our instrument in a specific channel and at the same time account for all the other photons which might have been emitted which *did not* result in a recorded event in USA. This can be thought of as an inversion problem: from the spectrum of counts obtained by the instrument we would like to know the spectrum of photons emitted by the astrophysical source.

In this report we describe the physics underlying the response of proportional counters as it is applicable to USA. We explain how we used ground and in-orbit calibration data of the characteristic photons from a radioactive $^{55}_{26}$Fe source to determine the calibration parameters. Finally we describe the procedure for building the USA *response matrices* and test these on USA observations of the well-known Crab nebula, to verify that the parameters we obtain are in agreement with what is known about the Crab from previous X-ray experiments.

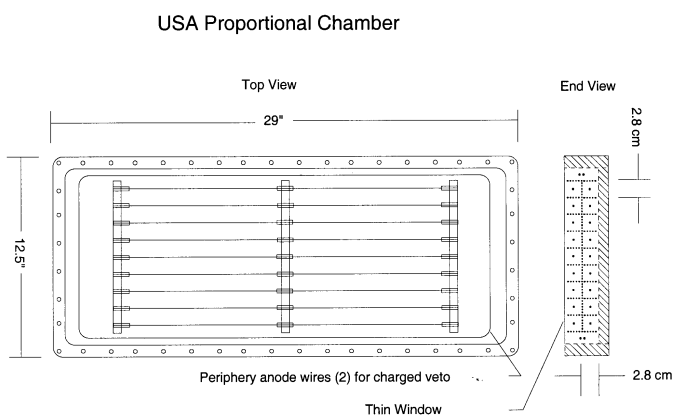

Fig. 3.— USA proportional chamber as viewed from the top. The active area of the proportional counter wire chamber is that area where the anode wires are directly illuminated by the cosmic sources through the thin window/collimator/heat shield combination. The area around the sides of the detector chamber where the perimeter wire resides is not directly illuminated and thus is not part of the effective source-detecting gas volume of USA. The active X-ray collecting area is (adjusting for the rounded corners in the heat shield frame) $9 \times 2.82\,\mathrm{cm} \times 59.6\,\mathrm{cm} = 1512.7\,\mathrm{cm}^2$. In the cut-away view on the right the mesh of grounding cathode wires that surround each anode wire is visible. This set of wires along with the nickel-chromium of the window and the bottom of the chamber interior serve as the ground plane the anode wire cells.

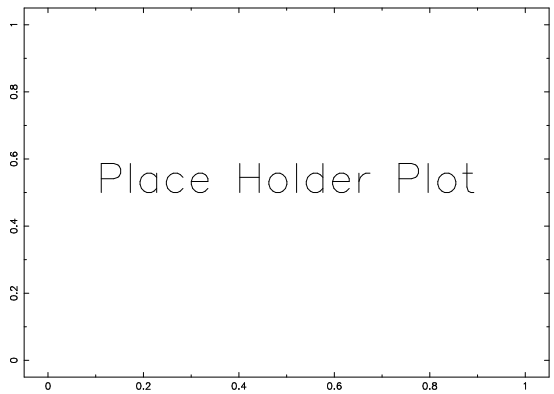

Fig. 4.— Exploded view of the USA collimator and proportional chamber showing many of the window and vignetting constituents of the detector design that will be discussed in this report. The depth of the *interior* of the wirechamber is not shown and is 2.44 inches (6.188 cm).

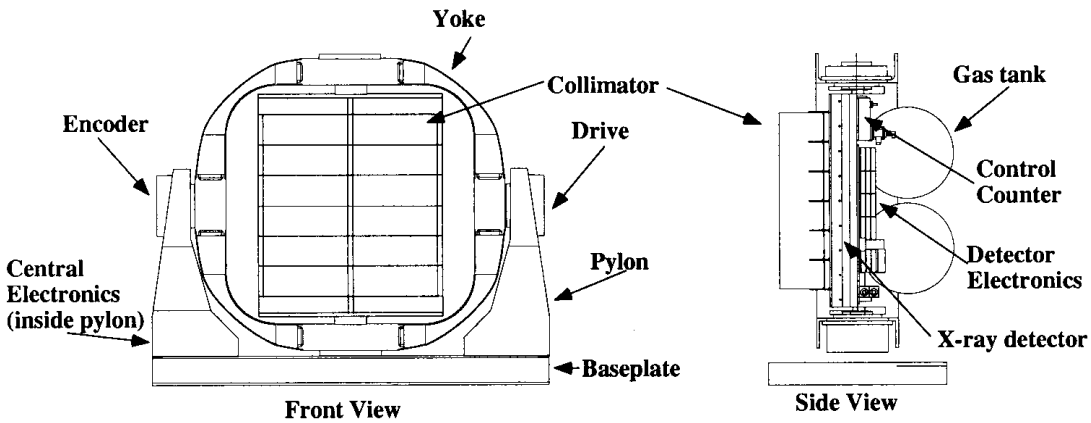

Fig. 5.— Two views of the USA experiment. In both orientations the body of the ARGOS space vehicle is located at the bottom of the figure, below USA.

2.2. The USA Response Model

Each detector consists of a multi-wire constant flow proportional chamber of roughly 1500 cm^2 total area (see Figures 3 and 4), covered with a Mylar heat shield, collimator, Nickel mesh, and thin Mylar window. The detector wire chamber is filled with P-10 gas held at a pressure of 15.5 psi (1.05 atm) at approximately room temperature. Precise absolute timing information is achieved using a GPS receiver on board ARGOS and timing resolution is 2μs or 32μs depending on the Detector Interface Board (DIB) mode (see Section 4.2 for details on the USA DIB observing modes). Figure 3 shows a detailed view of the USA proportional chamber, including the wire arrangement in the chamber, both layers, and the periphery anode wire which serves as part of the charged particle event veto system. Figure 5 shows a front and side view of the whole USA detector, including the pylon on which it is mounted to ARGOS. Table 1 summarizes the main technical characteristics of the USA instrument. For more information on ARGOS and USA see Ray et al. (2001).

We model the USA response to incoming X-ray photons with the following integral expression:

$$R_{ij} = \int_0^T \int_{E_{ij}^{min}}^{E_{ij}^{max}} \int_0^\infty \int_\Omega H(E_\gamma)\, C(\theta,\phi)\, M(E_\gamma)\, A\, W(E_\gamma)\, \eta_j(E_\gamma)\, P_j(E_\gamma;E)\, S(E_\gamma,\theta,\phi,t)\, d\Omega\, dE_\gamma\, dE\, dt, \tag{2}$$

where,

R_{ij}	=	Total photon interactions in PHA channel i and layer j in a time interval T,
E_γ	=	Energy of the incoming X-ray photon (units: keV),
E	=	Energy of the recorded photon event (units: keV),
E_{ij}^{min}	=	Minimum energy of channel i in layer j (units: keV),
E_{ij}^{max}	=	Maximum energy of channel i in layer j (units: keV),
$H(E_\gamma)$	=	Probability that a photon of energy E_γ will penetrate the USA heat shield,
$C(\theta,\phi)$	=	Angular response of USA on the sky,
$M(E_\gamma)$	=	Probability that a photon will penetrate the Nickel mesh,
A	=	Total geometrical area of a USA detector module (units: cm^2),
$W(E_\gamma)$	=	Probability that a photon of energy E_γ will penetrate the USA thin window,
$\eta_j(E_\gamma)$	=	Probability that a photon of energy E_γ will interact with the USA detector gas in layer j,
$P_j(E_\gamma,E)$	=	Probability that a photon of energy E_γ interacting with the USA gas in layer j will result in a pulse at energy E,
$S(E_\gamma,\theta,\phi,t)$	=	Source surface brightness spectrum on the sky as a function of time (units: photons/s-keV-str-cm^2).

R_{ij} gives the number of photon events in a USA detector module inside the energy range E_{ij}^{min} to E_{ij}^{max} in the time interval T. The index i designates the energy channel (raw "PHA" channel; see below) and j designates the wire chamber layer in which the detection occurred. Note that E_{i1}^{min} need not equal E_{i2}^{min} and likewise, E_{i1}^{max} need not equal E_{i2}^{max}.

The actual number of photons that can impinge on the USA detector and have a chance of producing a detectable pulse is first determined by the output of the celestial source. The source brightness distribution is given by $S(E_\gamma,\theta,\phi,t)$ and is a function of the incoming X-ray energy E_γ, the angular coordinates on the sky θ and ϕ, and the time, t. The convolution of S with the angular response of USA given by the collimator function $C(\theta,\phi)$ determines which photons can even make it to the window over the gas volume. For a point

source the function $C(\theta, \phi)$ reduces to a delta-function at the source coordinates so that $C(\theta, \phi)$ becomes $C(\alpha)$ where α is the angular distance of the collimator response peak from the source position. The USA collimator function is discussed below.

The function $P_j(E_\gamma, E)$ gives the probability that a X-ray photon of incoming energy E_γ will result in a detectable pulse at energy E. $P_j(E_\gamma, E)$ is a complex function of the gas physics of the P-10 mixture and how efficiently the induced charge densities are collected and will be described in Section 2.9.

Essentially, Equation 2 gives the number of electron-ion pair clouds that are created inside the USA wirechamber. The energy calibration of USA is a two-stage process. First, the response of the USA chamber gas must be modeled as a function of incoming photon energy using Equation 2 in order to understand the likely number of photon interactions inside the chamber during each observations. Second, the process of how the resulting electron-ion pairs are multiplied and collected must be modeled as accurately as possible using Equation 3 below.

2.3. USA Energy Gain Relation

Once a charge cloud is created and collected by the anode wire the resulting pulse must be translated into an energy for the original photon. Thus, we must model the multiplication and collection of the electron avalanches so that a mapping of charge cloud properties to photon energy can be achieved. Considerable research has been done to understand the process of charge avalanche multiplication and charge collection in proportional counters. The proportional counter will produce a signal proportional to the total number of electrons collected from the pair cloud. That is, we model the pulse height channel for a particular photon with the following linear relationship:

$$\text{PHA} \equiv \text{i} = G_{1j}\left[\frac{E_\gamma}{w(E_\gamma)}\right] + G_{0j}, \tag{3}$$

where G_{1j}, G_{0j} are themselves functions of the layer value (j) and $w(E)$ is a function of energy that gives the average amount of energy required to produce one electron-ion pair in the USA chamber gas for an incoming photon of energy E_γ. Equation 3 sets the boundaries E_{ij}^{min} and E_{ij}^{max} in Equation 2. The gain parameters G_{1j}, G_{0j} can vary with time over the life of the mission and we will find considerable evidence that they do so. Thus, we will model these two parameters also as linear functions of time:

$$G_{1j}(T_m) = g_{1j}^1\, T_m + g_{1j}^0\,, \tag{4}$$

and

$$G_{0j}(T_m) = g_{0j}^1\, T_m + g_{0j}^0\,, \tag{5}$$

where T_m is the number of days since January 1, 1999 and g_{1j}^1, g_{1j}^0, g_{0j}^1, and g_{0j}^0 are constants. The function $w(E_\gamma)$ gives the amount of energy needed to create an ion-electron pair by a photon of energy E_γ and is discussed in section 2.5 below. If there are losses of electrons after the cloud creation but before charge collection then these losses can interfere with the accurate recording of the original photon's energy. If the ion pair cloud is created to close to the thin window some of the ions may interact with the window and thus be lost to the charge collection process. This is the phenomenon of "partial charge collection" and we discuss it in Section 2.11.

2.4. Window Transmission For USA

A typical X-ray photon will first strike the USA heat shield of Mylar and Aluminum on its way into the wire chamber. The heat shield is designed to prevent heat loss from the detector module when it is pointed at deep space. A secondary function is to prevent direct sunlight from falling on the thin window and causing heat damage during the mission. Once the photon has passed through the heat shield it must move down the collimator without interacting with the collimator walls and penetrate the Nickel support mesh for the thin window (see Figure 4). The Nickel support mesh was measured in the laboratory as having a transmission of 84% at *optical* wavelengths. However, its thickness of $2.0 - 2.54 \times 10^{-3}$ cm makes it possible for some X-rays in the USA band to penetrate the nickel. The function $M(E_\gamma)$ is modeled in a manner similar to the way that the other window and heat shield components are modeled. The thin window is composed of Mylar and Nickel/Chromium ("Nichrome"). This Nichrome layer on the underside of the thin window serves as part of the ground plane for the high voltage activation of wire layer 1. It is the combination of the transmission of the heat shield and thin window that determines the low energy response of the USA instrument. The transmission of the heat shield, nickel mesh, and thin window are discussed in Section 2.4. Table 2 lists the different layers of material an incoming X-ray must traverse.

The heat shield penetration probability at energy E_γ is given by

$$H(E_\gamma) \;=\; \exp\left[-\left(\frac{\mu}{\rho}\right)_{Mylar}(E_\gamma)\;\rho(Mylar)\;L_{HS;Mylar} \;-\left(\frac{\mu}{\rho}\right)_{Al}(E_\gamma)\;\rho(Al)\;L_{HS;Al}\right] \tag{6}$$

where

$\left(\frac{\mu}{\rho}\right)_{Mylar}(E_\gamma)$	=	Photoelectric cross section of Mylar ($C_{10}H_4O_8$) as a function of photon energy,
$\left(\frac{\mu}{\rho}\right)_{Al}(E_\gamma)$	=	Photoelectric cross section of Aluminum as a function of photon energy,
$\rho(Mylar)$	=	Density of Mylar (1.380 g cm^{-3}),
$\rho(Al)$	=	Density of Aluminum (2.699 g cm^{-3}),
$L_{HS;Mylar}$	=	Thickness of the heat shield Mylar (see Table 1),
$L_{HS;Al}$	=	Thickness of the heat shield Aluminum (see Table 1).

The thin window penetration probability at energy E_γ is given by

$$W(E_\gamma) = \exp\left[-\left(\frac{\mu}{\rho}\right)_{Mylar}(E_\gamma)\;\rho(Mylar)\;L_{W;Mylar} \;-\left(\frac{\mu}{\rho}\right)_{Ni}(E_\gamma)\;\rho(Ni)\;w(Ni)\;L_{W;NiCr} \;-\left(\frac{\mu}{\rho}\right)_{Cr}(E_\gamma)\;\rho(Cr)\;w(Cr)\;L_{W;NiCr}\right]$$

where

$\left(\frac{\mu}{\rho}\right)_{NiCr}(E_\gamma)$	=	Photoelectric cross section of Nichrome as a function of photon energy,
$\rho(Ni)$	=	Density of Nickel (8.902 g cm^{-3}),
$w(Ni)$	=	Mass fraction of Nickel in 80/20 Nichrome (0.832),
$\rho(Cr)$	=	Density of Chromium (7.180 g cm^{-3}),
$w(Cr)$	=	Mass fraction of Chromium in 80/20 Nichrome (0.168),

$L_{W;Mylar}$	=	Thickness of the window Mylar (see Table 1),
$L_{W;NiCr}$	=	Thickness of the window Nichrome (see Table 1).

The photoelectric cross sections and mass densities for each component were taken from the National Institutes of Standards and Technology web site at URL: http://physics.nist.gov/PhysRefData/.

In Figure 8 we show the resulting transmission function values as a function of energy. We include in the figure a number of details for each USA component so that the affects of each component can be understood individually. The total transmission function, that does not include the effects of collimator transmission, is also shown in the figure. In order to compute the transmission of the nickel mesh we assume that 84% of all incoming photons will penetrate the mesh simply because the will not strike any nickel at all. The remaining 16% of the X-ray photons are assumed to fall on uniform thickness nickel wires 25.4 [$=L(Ni)$ μm] in thickness. Thus, the nickel mesh transmission expression is

$$M(E_\gamma) = 0.84 \ + \ 0.16 \exp\left[- \left(\frac{\mu}{\rho}\right)_{Ni} (E_\gamma) \ \rho(Ni) \ L(Ni) \right]. \tag{7}$$

2.5. Energy To Create One Electron-Ion Pair

The value of $\frac{E_\gamma}{w(E_\gamma)}$ gives the average number of ion-electron pairs created by a photon of energy E_γ. Experiment has shown that this number of is different for different counter gases. Also, due to various value of $w(E)$ can vary by as much as 10% over the energy range of the USA detectors and we must make allowance for this variation in our response model. The variation of the value of $w(E)$ is shown in Figure 6 along with the data for Argon from Monteiro et al. (2003). In the USA wire chamber we model the variation of $w(E)$ as

$$w(E) \ = \ W_0 f \ + \ W(E)(1-f)\,, \tag{8}$$

where W_0 is the mean value over the USA energy range, $W(E)$ is a linear fit to the data points from Monteiro et al. (2003) for Argon, and f is a constant that weighs the relative contributions of W_0 and $W(E)$. Experimenting with the USA Crab calibration observations has shown that a values of $W_0 = 26.4$ eV and $f = 0.4$ gives the best results for the USA P-10 gas mixture.

2.6. P-10 Gas Interaction Probability

Once an X-ray has penetrated into the wire chamber, if it is to produce a detectable pulse it must interact with the P-10 gas in order to create a cloud of electron-ion pairs by photoionizing some of the P-10 gas constituents. The function $\eta_j(E_\gamma)$ gives the probability that the X-ray photon will yield an electron-ion pair cloud somewhere in the active gas volume of layer j. If an pair cloud is created we assume the electrons will drift toward the anode wire and the ions will drift toward the cathode (ground) wires.

The gas interaction probability $\eta_j(E_\gamma)$ is the probability that once a X-ray photon enters the USA gas volume and then ionizes either an ^{40}Ar atom or a CH_4 molecule creating an ion-electron pair that can result in charge multiplication and a detectable pulse. We assume that if an electron-ion pair is created in the volume specific to a particular anode wire then all electrons created in the multiplication process will drift toward that anode wire and all ions created will drift toward its respective ground planes (i.e., there is no

Feature		Reference or Report Section
Gas:	P-10 (90% Argon, 10% Methane)	Section 2.6
Energy Range:	1-15 keV	Section 2.6
Energy Resolution:	∼17% (1 keV @ 5.9 keV)	Section 2.10
In-orbit calibration:	solenoid operated $^{55}_{26}$Fe source	Section 3
Effective Area:	~ 1000 cm^2 @ 3keV	Figure 10, Section 2.8
Active Detector Volume:	25.2 cm × 5.6 cm × 60 cm	Section 2.1
1 Crab	~ 3900 cts s^{-1}	Section 4.3
Background:	$\sim 20 - 50$ cts s^{-1}	Appendix on background in Wen (1997)
Operating Voltage:	2776 volts	
Field of view:	Collimation of 1.2° FWHM Cone	Appendix on collimators in Wen (1997)
	0.05° flat top	
Heat Shield:	2.0 μm Mylar	USA Fabrication Documentation
	800.0 Å Aluminum	
Nickel Mesh:	25.4 μm	USA Fabrication Documentation
Window:	5.0 μm Mylar	USA Fabrication Documentation
	30.0 Å Nickel-Chromium	
Timing Resolution:	2 μs, 32 μs, or 10 ms	Ray et al. (2001)
Deadtime:	$\tau = 16.4\,\mu$s	Shabad (2000)

Table 1: Summary of USA instrument characteristics.

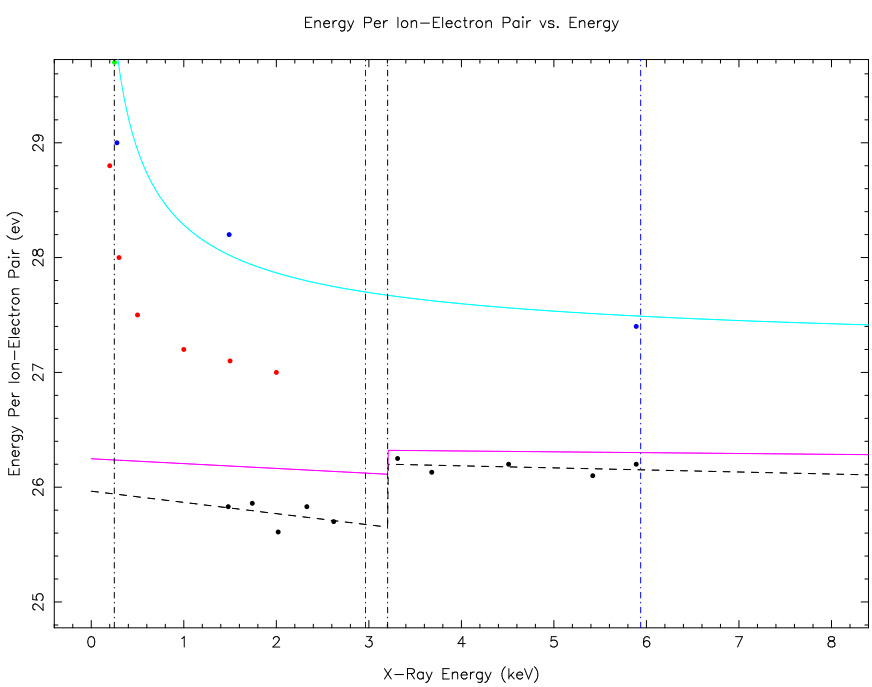

Fig. 6.— The value of the function $w(E)$ for various gasses used in proportional counters. The solid red line near 26 eV shows the combined W-values for the Argon/Methane P-10 gas over the USA energy range.

Constituent	Material or Chemical formula	Thickness
Heat Shield	Mylar ($C_{10}H_8O_4$)	2.0 μm
Heat Shield	Aluminum (Al)	800 Å
Nickel Mesh	Fine Nickel wire	25.4 μm (see text)
Thin Window	Mylar ($C_{10}H_8O_4$)	5.0 μm
Thin Window	Nichrome (80/20)	30 Å
P-10 Gas	90% Ar + 10% CH_4	6.188 cm

Table 2: USA materials for the heat shield, thin window, and both wire layers.

electron-ion drift "cross talk" between layers and anode wire volumes). Any cross-talk between anode wires or layers would result in X-ray photon self-veto counts. An estimate of the fraction of all incoming photons that lead to vetos is not currently part of the working model for the USA response. The probability $\eta_j(E_\gamma)$ will depend on the properties of the gas used for the detection and will vary dramatically depending on the energy of the incoming photon.

The gas used in USA is P-10, that is 90% Argon (by number) and 10% Methane (CH_4). The probability that an X-ray photon of energy E_γ that enters the gas chamber will interact with the gas ionizing either an Argon atom or a Methane molecule in layer 1 only is given by

$$\eta_1(E_\gamma) = 1 - \exp\left[-\left(\frac{\mu}{\rho}\right)_{Ar}(E_\gamma)\ \rho(Ar)\ w(Ar)\ L_1\ -\left(\frac{\mu}{\rho}\right)_{CH_4}(E_\gamma)\ \rho(CH_4)\ w(CH_4)\ L_1\right] \tag{9}$$

where

$\left(\frac{\mu}{\rho}\right)_{Ar}(E_\gamma)$ = Photoelectric cross section of ^{40}Ar as a function of photon energy,
$\rho(Ar)$ = Density of P-10 at 1.1 psia (0.001772 g cm^{-3}),
$w(Ar)$ = Mass fraction of Argon in P-10 gas (0.9573),
$w(CH_4)$ = Mass fraction of Methane in P-10 gas (0.04267),
L_1 = Depth of Layer 1 (see Table 1).

The probability that an X-ray photon of energy E_γ that penetrates into the detector gas volume will ionize either an Argon atom or a Methane molecule in either of layer 1 or layer 2 is given by

$$\eta_{12}(E_\gamma) = 1 - \exp\left[-\left(\frac{\mu}{\rho}\right)_{Ar}(E_\gamma)\ \rho(Ar)\ w(Ar)\ L_{12}\ -\left(\frac{\mu}{\rho}\right)_{CH_4}(E_\gamma)\ \rho(CH_4)\ w(CH_4)\ L_{12}\right] \tag{10}$$

where

L_{12} = Total depth of USA gas volume (see Table 1)

We refer to the function of energy given by the product

$$\epsilon_j(E_\gamma) \ = \ H(E_\gamma)\ W(E_\gamma)\ M(E_\gamma)\ \eta_j(E_\gamma) \tag{11}$$

as the *interaction probability* of the photon of energy E_γ. $\epsilon_j(E_\gamma)$ gives the probability that a photon of energy E_γ headed straight into the USA detector active volume will produce an ion-electron pair cloud that can be detected as an event. The function $\eta_j(E_\gamma)$ is shown in Figure 7 for layers 1, 2 and sum of layers 1 and 2. We show the total transmission of the heat shield-window-mesh-collimator (see below) combination in Figure 8. It is interesting to note that the Nickel mesh becomes partially transparent at an energy below Nickel K-edge at 8.3328 keV resulting in a discontinuity at this energy. Furthermore, as the X-ray energy goes up Nickel becomes progressively more transparent to photons and the throughput of the mesh increases above the nominal 84% measured in the laboratory.

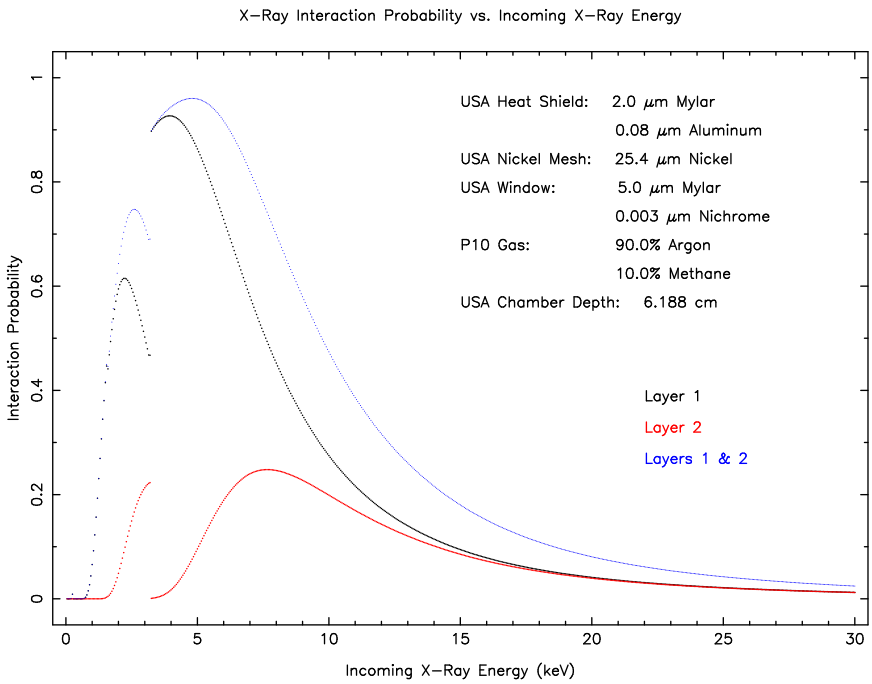

Fig. 7.— USA P-10 gas X-ray interaction probabilities as a function of incoming photon energy: Layers 1, 2, and combined 1 and 2. The prominent edge at 3.2029 keV results from photons above this energy having sufficient energy to ionize K-shell electrons in Argon.

2.7. USA Collimator Response

For each USA detector the collimator consisted of a copper hexagonal mesh 4.5 inches high covering the active area of the proportional chamber (see Figure 4). Each detector collimator module was constructed from eight separate collimator sections built at the Stanford Linear Accelerator Center (SLAC) (Wen 1997). The angular response of one collimator section is shown in Figure 9. This represents the function $C(\theta, \phi)$ but under the assumption that the only angular dependence of the response is with angular distance away from the collimator axis. In this case $C(\theta, \phi)$ reduces to $C(\alpha)$ where α is the angular distance from the center of the USA look direction. The USA response has a small flat top with a sharp descent as the angle off source increased giving the FWHM of ~ 1.22 deg (Wen 1997). The fraction of the USA active volume that the collimator covers is about 0.952 if one looks right down the observational axis of the instrument. For point sources, if the source X-rays land on the sides of the angular response, the count rate will be

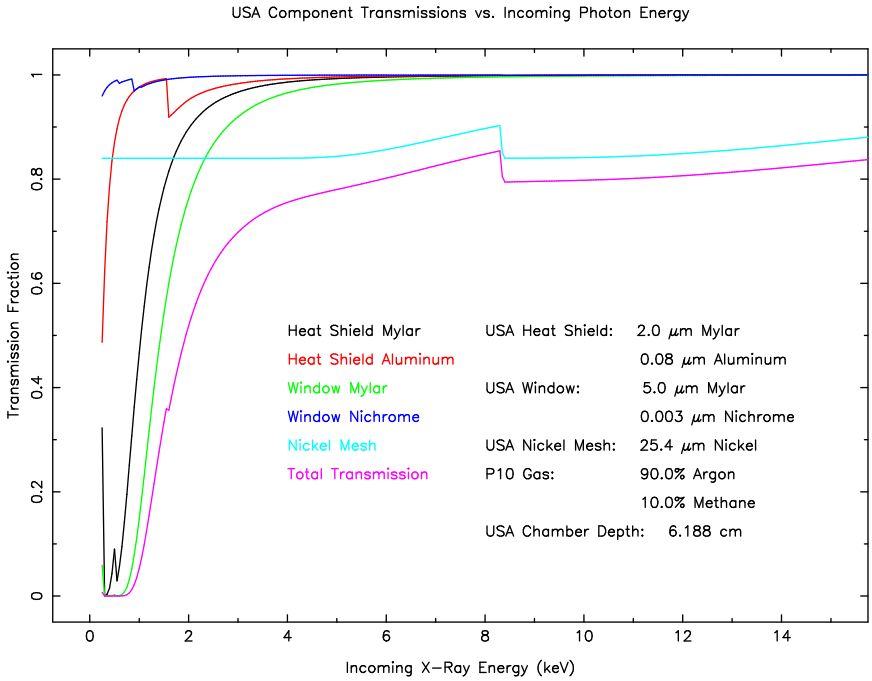

Fig. 8.— The fractional transmission values as a function of energy for the USA constituents as listed in the figure.

diminished by the factor given in Figure 9. However, if the source has significant variations in brightness on size scales near or larger than the 1.22 deg FWHM then the convolution of $S(E_\gamma, \theta, \phi, t)$ with $C(\theta, \phi)$ will increase the complexity of the interpretation of the count rates as a function of time. In this report, we use the Crab pulsar and Nebula as our calibration source. Its angular extent on the sky is only $\sim$ 100 arcsec and the interplay of $S(E_\gamma, \theta, \phi, t)$ with $C(\theta, \phi)$ should not present any difficulties and reducing C to $C(\alpha)$ is an adequate approximation.

2.8. USA Effective area

The effective area of the instrument is obtained by multiplying the interaction probability $\epsilon_j(E_\gamma)$ by the geometrical area of each detector, then by the Nickel mesh transmission, and finally by the collimator response. We take the collimator response to be simply the maximum of the curve given in Figure 9 or 0.9520. The total geometrical area of one detector is 1512.7 cm^2. The resulting USA Effective Area curve as a function of energy is shown in Figure 10. The large discontinuity at 3.2 keV is simply the Argon K-edge. There is also a slight Nickel K-edge discontinuity at 8.33 keV.

2.9. Argon Escape Peak

When a 1-15 keV X-ray photon enters the USA gas chamber it can either interact with the P-10 gas by photoionizing one of the gas constituents or it can pass all the way through the chamber and hit the Aluminum back wall. If the photon hits the back wall it is not likely to produce any photoelectric electrons

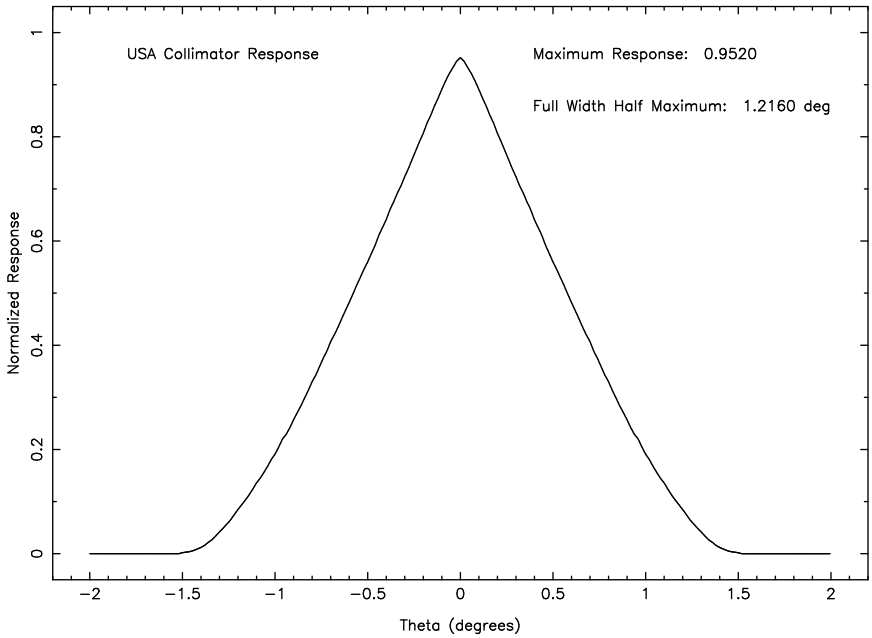

Fig. 9.— USA collimator response on the sky as a function of incoming photon angle away from exactly parallel to the instrument observational axis.

since its energy is so much higher than the work function of Aluminum (4.28 eV). Such photons tend to penetrate well into the metal surface and not induce any electrons emerging into the chamber. Thus, X-rays that go all the way through the chamber will most likely be lost and not recorded. If the photon has an energy $E_\gamma < 3.2029$ keV and it does interact with the gas it will most likely photoionize either an L-shell electron in Argon or a K-shell electron in the Carbon in the Methane. Either of these possibilities leads to the creation of an electron-ion pair and a possible photon event recorded by USA. If an X-ray photon with energy $E_\gamma > 3.2029$ keV interacts with the P-10 gas it will most likely ionize a K-shell electron from the Argon leaving the Argon atom in a state of Ar^+ with a "hole" in the K-shell. At this point, the Ar^+ atom can either Auger ionize by an internal re-arrangement of its electron configuration resulting in the ejection of another electron that contributes to the energy of the original photopeak, or the Ar^+ atom can undergo a radiative transition where an electron in the L-shell de-excites to fill the K-shell hole producing either a $E(K_\alpha) = 2.956$ keV or $E(K_\beta) = 3.190$ keV photon emerging into the gas chamber. If this radiated de-excitation photon escapes from the wire chamber entirely a loss of energy from the original E_γ photopeak comes about and USA registers a X-ray event at energy $E_{es} = E_\gamma - E(K_{\alpha\beta})$ instead of E_γ. This is the "escape peak" that is characteristic of proportional counter detectors. In order to properly model the response of the USA detector to incoming photons it is necessary to understand the nature and size of this escape peak in USA X-ray spectra.

The de-excitation of an Argon L-shell electron to fill the K-shell hole is called "fluorescence" and it occurs a fraction $\omega_F = 0.122$ of the time under ideal conditions (Bambynek et al. 1972). This means that for a beam of monochromatic X-rays of number flux I_o, USA will record a fraction $(1 - \omega_F)\, I_o$ of events at the original photon energy E_γ and a fraction $\omega_F\, I_o$ events at energy $E_\gamma - E(K_{\alpha\beta})$ to account for the escape of the $K_{\alpha\beta}$ photons from the chamber. For this reason, we expect the $^{55}_{26}$Fe calibration source to produce four peaks: two main peaks at roughly 5.893 keV and 6.490 keV (see Table 3) along with their respective (and

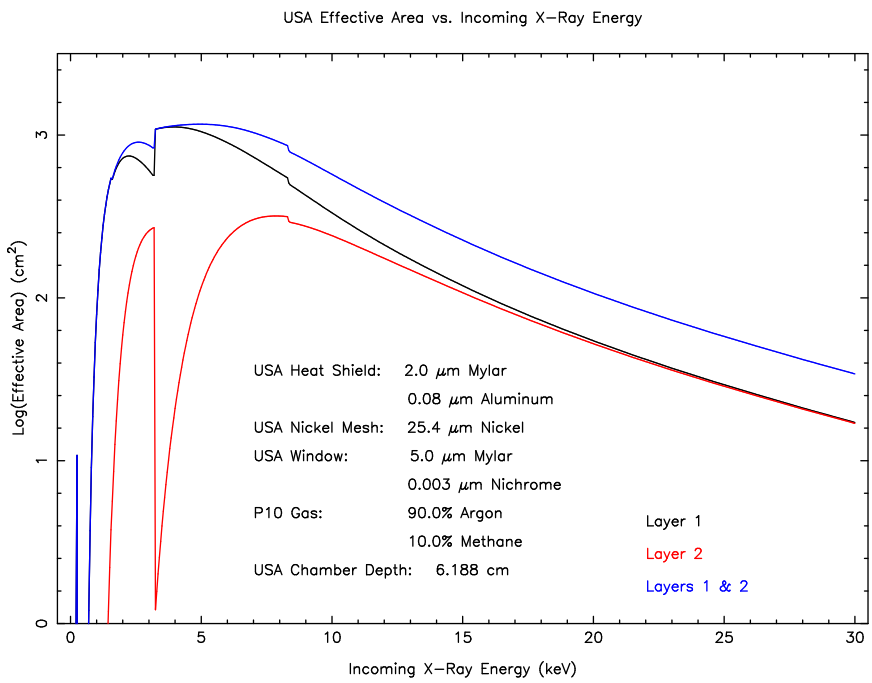

Fig. 10.— The USA Effective Area as a function of incoming photon energy: Layers 1, 2, and combined 1 & 2. In addition to the well known Argon K-edge at 3.2 keV there is a small Nickel K-edge at 8.33 keV.

much smaller) escape peaks. One of the parameters to be derived from our calibration will be the fraction of photon event detected in the escape peak, which is a number on the order of 5–10%. See Appendix 6 for more details on the accounting for the amplitude of the Argon escape peak.

An ideal radiation detector would allow us to measure the energy of an incoming photon with exact precision; In other words, if we bombarded our detector with a beam of monoenergetic photons, the *detector response* is a delta function. Due to the stochastic nature of this ionization process, however, the response of the detector to a monoenergetic source of photons is a finite width distribution of pulse heights, rather than a pure delta function. For photons with original energies $E_\gamma < E(\text{Argon K-edge})$, because there is no escape peak, the model for the Pulse Height Amplitude (PHA) distribution will be a single gaussian:

$$P(E_\gamma; E) = \frac{A}{\sigma\sqrt{2\pi}} \exp(-\frac{(E-E_\gamma)^2}{2\sigma^2}) \tag{12}$$

to account for the spread of recorded photon energies around the incoming energy E_γ. The width of the peak, σ, is a function of energy and is discussed in the next section. If $E_\gamma \geq E(\text{Argon K-edge})$ we use two gaussians:

$$P(E_\gamma; E) = \frac{A_1}{\sigma_1\sqrt{2\pi}} \exp(-\frac{(E-E_\gamma)^2}{2\sigma_1^2}) + \frac{A_2}{\sigma_2\sqrt{2\pi}} \exp(-\frac{(E-E_\gamma-E_{es})^2}{2\sigma_2^2}) \tag{13}$$

In this expression, E_{es} is the energy of the escaping photon and the values of A_1, A_2, σ_1, and σ_2 must be measured experimentally as a part of the USA calibration. $P(E_\gamma, E)$ is always normalized so that

$$\int_0^\infty P(E_\gamma; E) dE_\gamma \leq 1 \tag{14}$$

This point is discussed further in Appendix 6.

2.10. USA Energy Resolution

As was discussed in the previous section, real detectors have far from perfect delta function energy resolution. It is standard to define the (fractional) resolution of a detector at a given energy as the ratio of the full width at half maximum (FWHM) to the average pulse height $H_\circ$ at that energy, as seen in Figure 11. The closer this distribution is to a delta function, the better we say its *resolution* is. The two main factors limiting the resolution of a proportional counter are variations in the number of electron-ion pairs produced by incoming photons of the same energy, and variations in the resulting single-electron avalanche magnitudes.

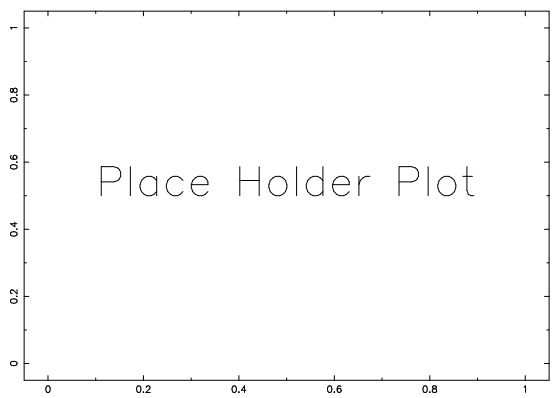

Fig. 11.— The definition of Energy Resolution. The value of the function $\frac{dN}{dH}$ as a function of pulse heights H gives the distribution of pulse height amplitudes resulting from statistical fluctuations in the real detector response. [from Knoll (2000)]

The overall resolution limit of a proportional counter can then be expressed as:

$$R = 2.35\sqrt{\frac{W\,(F+b)}{E_\gamma}}, \tag{15}$$

W represents the energy required to form one electron-ion pair, F is a number referred to as the "Fano Factor", and b is sometimes referred to as the "multiplication variance". For P-10 gas, these constants have been measured to be: W=26 eV (its average over the 1-15 keV band), F=0.17, and b=0.5 (Knoll 2000), yielding

$$R = \frac{0.31}{\sqrt{E_\gamma}} = 2.35\,\frac{\sigma(E_\gamma)}{E_\gamma}. \tag{16}$$

Furthermore, other factors such as imperfections in the anode wire and noisy electronics will contribute to make the resolution in the USA detector worse than this ideal statistical limit. We will, nevertheless, model the resolution of USA as the inverse square root of the photon energy, though the normalization constant will be greater than 0.31 and will be obtained from the calibration data.

2.11. Partial Charge Collection

If the mean free path of X-ray photons in the P-10 gas becomes very short then a significant number of photons produce electron-ion pair clouds very close to the Mylar window. In this case some of the charge clouds diffusively expand in close enough to the window for some of the electrons to come in contact with

the window. Those electrons that do contact the window will be lost from the charge collection process since they will never reach the anode wire. Inoue et al. (1978) analyzed this process in the case of Xenon-filled gas scintillation proportional counter and found that when the ratio $\kappa = \frac{D}{u\lambda} > 0.1$, where D is the electron diffusion coefficient, u is the electron drift velocity, and λ is the photon mean free path, the effects of partial charge collection became promenent in their experimental setup. Jahoda & McCammon (1988) adapted the Inoue et al. analysis to regular proportional counters with P-10 gas and found that partial charge collection are very important at energies below 1 keV but did not extend their analysis to higher energies. However, when analyzing the response of the Proportional Counter Array on the Rossi X-Ray Timing Explorer satellite Jahoda et al. (2003) found that partial charge collection effects played an important role in determining how many, and of what energy, electrons did make it to the anode wire. If the electron pair cloud has n_0 initial electrons then the number n that reach the anode is given by

$$f(n)\,dn \;=\; \kappa\,(1 - n/n_0)^{\kappa-1}\;dn. \tag{17}$$

The effects of partial charge collection are included in our model for the number of electrons that reach the multiplication region in 3.

3. The Energy Calibration of USA

The energy calibration of USA was carried out in several stages. Data were used from test spectra recorded on the ground using the $^{55}_{26}$Fe source over the course of several years. Some calibration data were taken in 1996, before the Detector Interface Board (DIB) was in place. This produced the highest resolution (128 channels) possible. The observations were taken at different voltages, so we made sure the data we used were at the same nominal high voltage as in orbit, that is 2776.5 V. Later ground data were taken in August, September, and October of 1997 and in June of 1998, with the DIB in place. All the ground data were used to derive an initial calibration which was then verified with data taken in orbit. The calibration in orbit was done using observations of blank sky with the $^{55}_{26}$Fe source temporarily placed in the field of view. Calibration in orbit introduced the added complication of subtracting the background (diffuse X-ray and particle-induced). Furthermore, by the time of USA's mission, the $^{55}_{26}$Fe source count rate was reduced to a rate of about 50-60 cts/sec compared to an initial rate of several thousand counts per second when the source was originally purchased (see next section). Finally, in order to measure the USA spectral response over the broadest range possible, the Crab pulsar, which has a well understood energy spectrum, was observed while on-orbit.

3.1. Calibration Sources

The source of photons used for the ground calibration is an iron ($^{55}_{26}$Fe) source. The iron source has a half-life of 2.73 years and through electron capture decays to $^{55}_{25}$Mn* (equation 18). The excited Mn atom then relaxes to the ground state by filling the vacancy in the inner orbit with an outer electron and producing an X-ray photon. It is these X-ray photons that we use as our calibration signal.

$$^{55}_{26}Fe + e^- \rightarrow^{55}_{25} Mn^* + \nu \rightarrow^{55}_{25} Mn + \gamma \tag{18}$$

Table 3 summarizes the three main transitions with their relative intensities (Browne, E. and Firestone, R. B. 1986).

Name	Transition	Energy (keV)	Relative Intensity
K_{α_1}	$2^2P_{3/2} \rightarrow 1^2S_{1/2}$ $(n = 2 \rightarrow n = 1)$	5.898	100
K_{α_2}	$2^2P_{1/2} \rightarrow 1^2S_{1/2}$ $(n = 2 \rightarrow n = 1)$	5.887	51
K_{β_1}	$3^2P \rightarrow 1^2S_{1/2}$ $(n = 3 \rightarrow n = 1)$	6.490	16

Table 3: Radioactive transitions of the $^{55}_{25}$Mn atom

3.2. On-ground calibration

3.2.1. 1996 Ground Data

Figure 12 shows a fit to some 1996 ground data. The two main gaussians, in red and blue, represent iron lines at 5.9 keV (which is actually a blend of two lines of very similar energies) and 6.5 keV (see table 3), as observed in layer 1 of the detector. The mean, 43.66 and 48.14 respectively, is expressed in channels out of 128. Figure 13 shows the best fit to the layer 2 spectrum. Once again, we see the main peak at 5.9 keV, and a smaller one at 6.5 keV, along with the corresponding escape peaks.

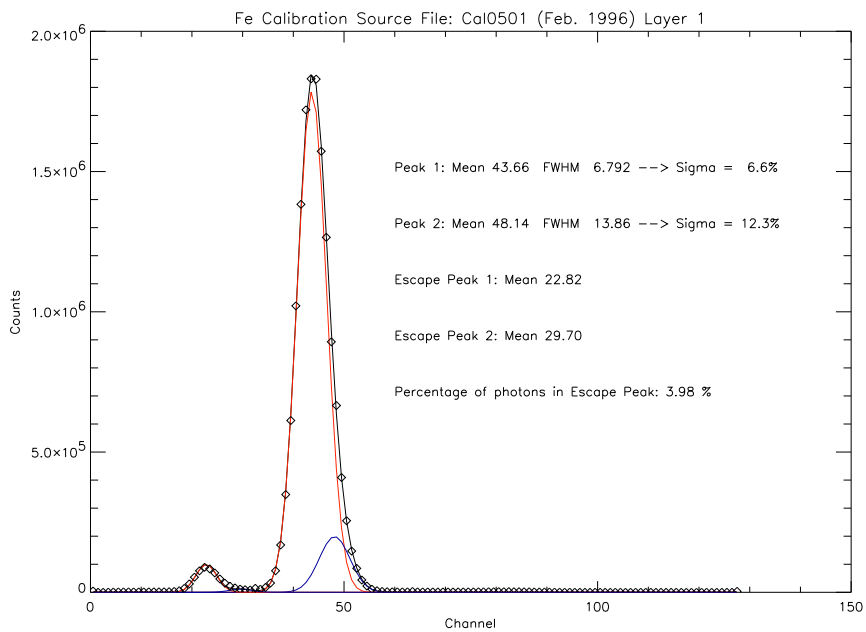

Fig. 12.— Fe calibration source (2 lines): Layer 1

Given the limited resolution of our in-orbit data, it becomes hard to fit the calibration data with four gaussians. We therefore decided to fit only one main peak and its escape peak. Figures 14 and 15 show such a fit to the same data as that shown in figures 12 and 13. Using the relative intensities of the lines (from table 3) we arrive at a mean energy of 5.8943 keV for the blend of the three lines.

As can be seen from the figures, the result of considering the spectrum as one gaussian instead of two is to effectively shift the line up to a slightly higher energy (5.95 vs 5.9) and increase the standard deviation of the gaussian by a small amount.

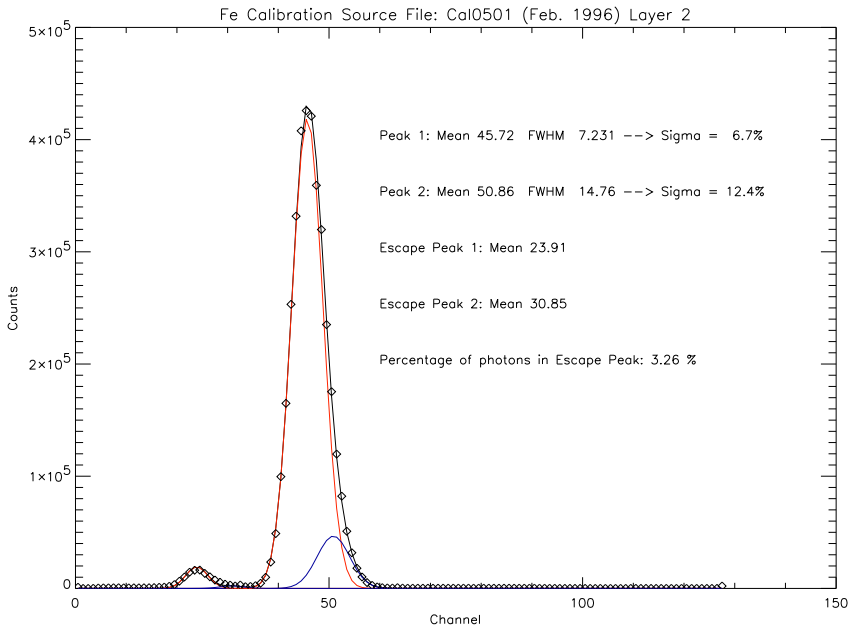

Fig. 13.— Fe calibration source (2 lines): Layer 2

3.2.2. 1997 Ground Data

Figures 16 and 17 show a fit to some 1997 ground data (layers 1 and 2 respectively). These data were taken with the DIB already in place, and therefore the number of channels is now greatly reduced (16 vs 128). One key difference with the 1996 ground data is the location of the iron peak. In figure 16 we find the mean in channel 6.40 (figure 17 shows layer 2 peaking in channel 6.07). By comparison the 1996 observations show the layer 1 peak (see figure 14) in channel 44.09 (or channel 5.51 in a 16 channel scale), and the layer 2 peak (see figure 15) in channel 46.21 (5.78 in a 16 channel scale). Even more confusing is the fact that some 1997 data (see figure 18) shows the layer 1 peak in channel 5.47.

3.2.3. 1998 Ground Data

We also looked at some TVAC data taken in June of 1998. As with the 1997 data, given the poor resolution (16 channels), we decided to fit the energy spectrum of the calibration source with only two gaussians: one for the main peak at 5.89 keV and one for the escape peak.

Figures 18 and 19 show the fits to the layer 1 and layer 2 spectra respectively. Once again, the key parameter to notice is the channel where the energy spectrum peaks. Figures 18 and 19 show the layer 1 spectrum peaking in channel 6.52, and the layer 2 spectrum peaks in channel 6.28. This is in conflict with the results obtained from the 1996 data and some of the 1997 data, but agrees with some of the 1997 ground data. It appears that the iron line in layer 1 of our detector varies its position from around channel 5.5 to 6.5.

By combining all available ground data from February 1996 (14 observations) and fitting a line to the

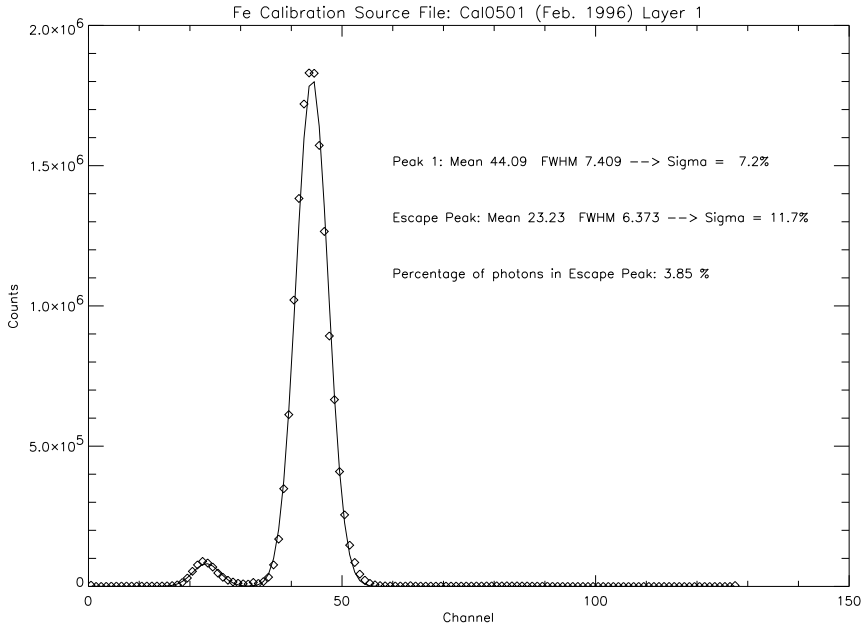

Fig. 14.— Fe calibration source: Layer 1

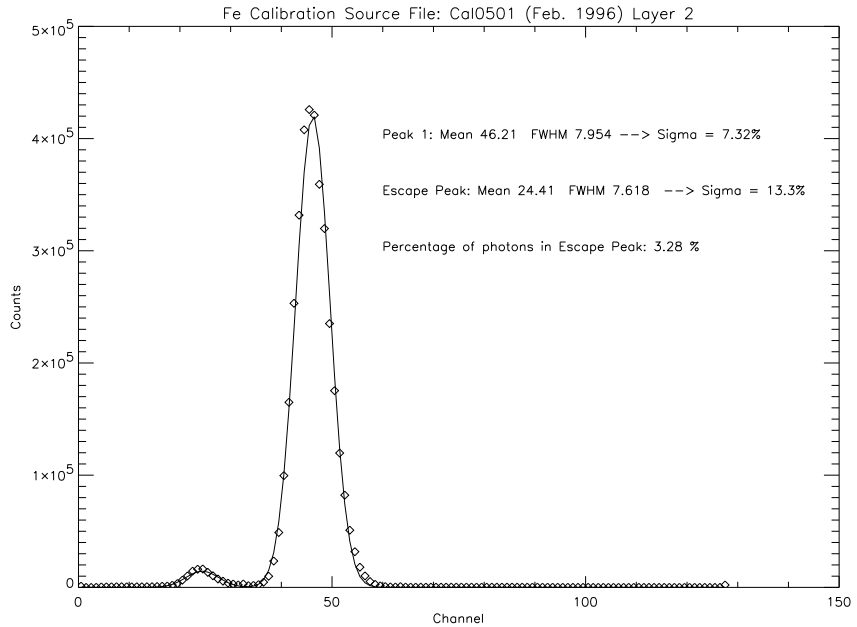

Fig. 15.— Fe calibration source: Layer 2

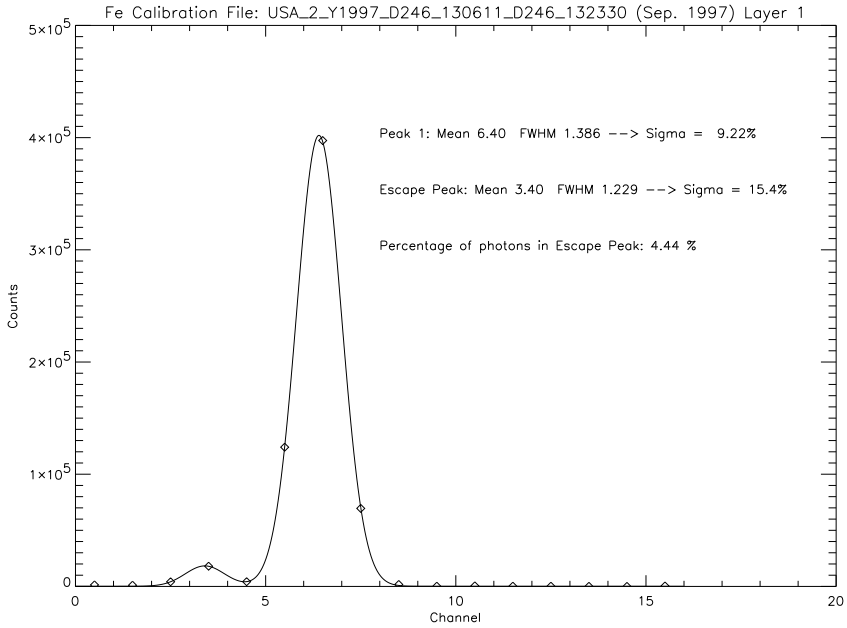

Fig. 16.— Fe Source 1997 TVAC : Layer 1

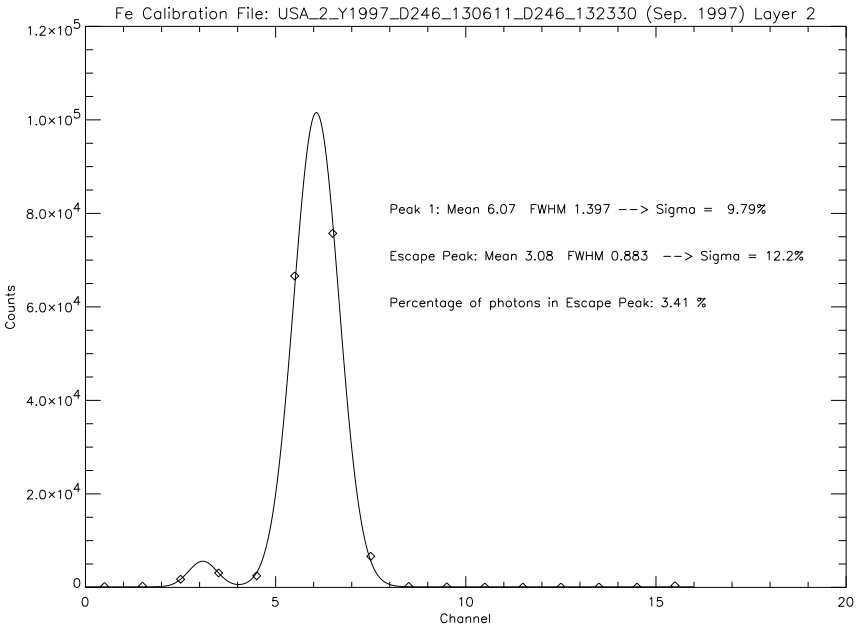

Fig. 17.— Fe Source 1997 TVAC : Layer 2

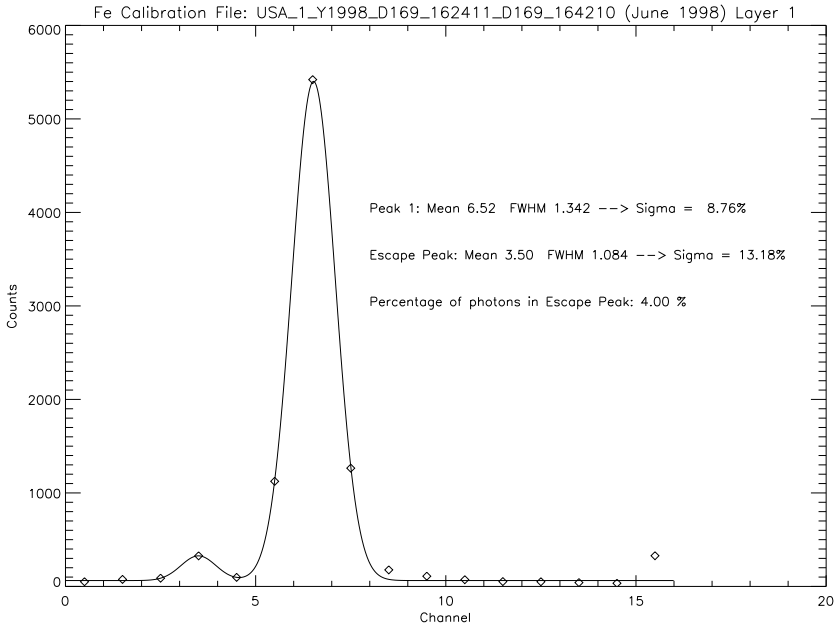

Fig. 18.— Fe Source 1998 TVAC : Layer 1

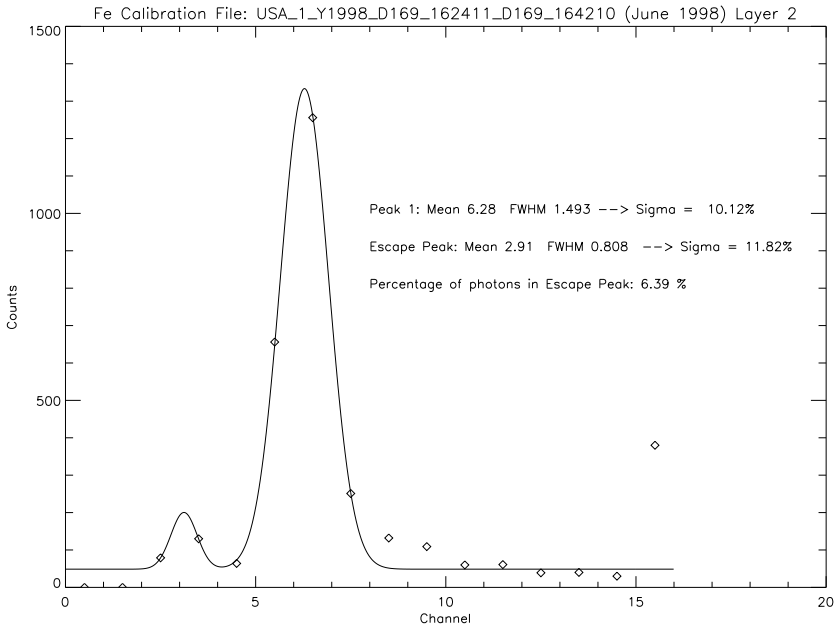

Fig. 19.— Fe Source 1998 TVAC : Layer 2

main peak and escape peaks of the iron line, we obtain an energy to channel conversion equation with the parameters listed in Table 4.

3.3. On-Orbit calibration

Once USA was in orbit, the calibration of the instrument could be verified and, if necessary, improved. For this task, we analyzed observations of the iron calibration source as it was placed in front of the detector while pointing at a blank part of the X-ray sky. The following figures show two typical calibration observations taken in orbit. The first one is taken on the ascending side of the orbit, while the second is taken on the descending part of the orbit. The observations normally consist of roughly 80 seconds of blank sky, followed by about 100 seconds of calibration ($^{55}_{26}$Fe) source. For each observation we obtained a rough estimate of the background in each layer, subtracted this background and then fit a gaussian to the resulting spectrum. As can be seen from these two observations, the peak in layer 1 falls about one channel higher in the ascending observation than in the descending one - a 20% difference in gain. Layer 2 does not show this dramatic difference.

3.4. DIB Mode 2

In Figure 22 we plot the location of the gaussian peak obtained from fitting the layer 1 spectra as described in the previous section to about 75 individual calibration observations. Each point represents one of these calibration observations. While there are large gaps in the coverage, the observations span roughly 400 days. In red we show the ascending observations and in blue the descending ones. These form two distinct populations. Figure 23 shows the same information for layer 2 where the effect is not so pronounced.

3.4.1. 8 keV Fluorescence Line

In the fits to the ^{55}Fe calibration observations done in orbit there is a persistent feature that shows up as a broad line at $\sim$ 8 keV (see Figures 27 and 26). In the calibration spectra taken in DIB mode 2 a feature is also present at roughly the same energy (see Figure 24). There are two possible explanations for this feature. First, the interaction of the charged particle environment with the USA collimator, which is made of copper (see Section 1) can produce an 8.03 keV Browne, E. and Firestone, R. B. (1986) fluorescence line that might be visible in the USA blank sky observations. In order to try and understand the possible origin of the observed line, in figure 25 we plot the ratio of counts in channels 5-7 (which is where the

Layer 1	*Offset*	*Linear*	*Quadratic*
	-0.2888	0.1417	-
Layer 2	*Offset*	*Linear*	*Quadratic*
	-0.3009	0.1358	-

Table 4: Gain parameters: Energy (keV) to Channel (128) fit (ground)

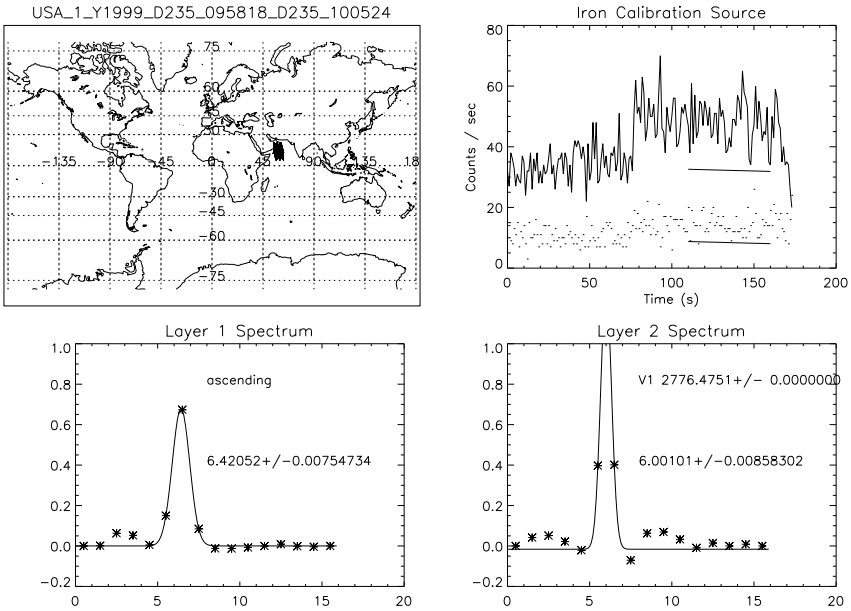

Fig. 20.— Typical Ascending Observation

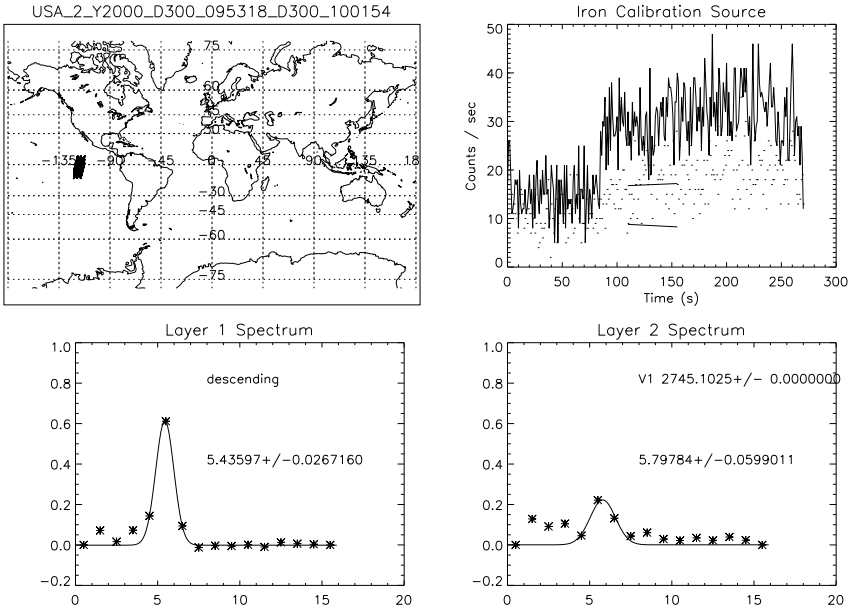

Fig. 21.— Typical Descending Observation

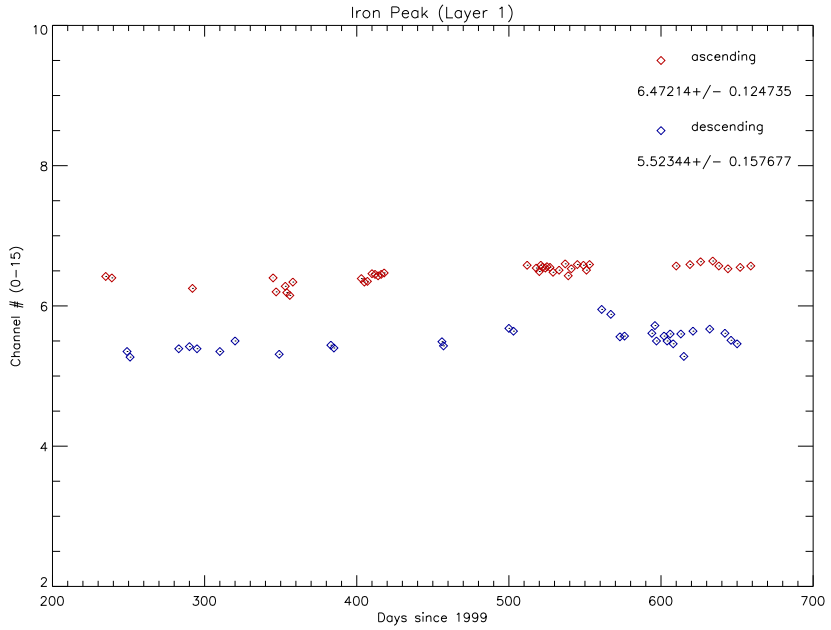

Fig. 22.— Fe Calibration Peak: Layer 1

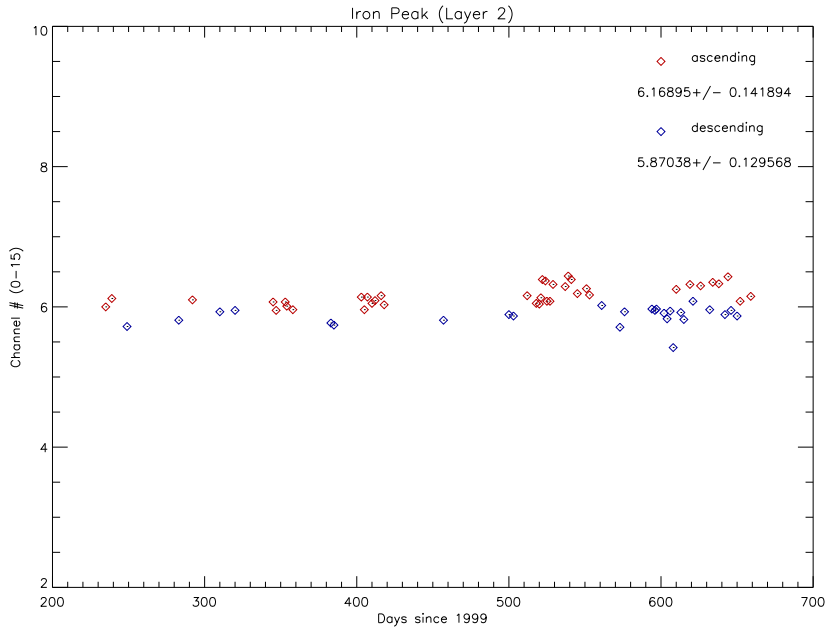

Fig. 23.— Fe Calibration Peak: Layer 2

copper peak roughly lies) to total counts versus the difference between counts in both layers of channel 15, which is a measure of the intensity of low energy electrons hitting the front window. The plot shows a mild correlation between the intensity of this line and the rate of soft electrons hitting the detector. Another possible explanation of the presence of this line can be seen by noting the nickel edge at 8.33 keV in Figure 8. The line may result from the increased transmission near this energy of the nickel mesh.

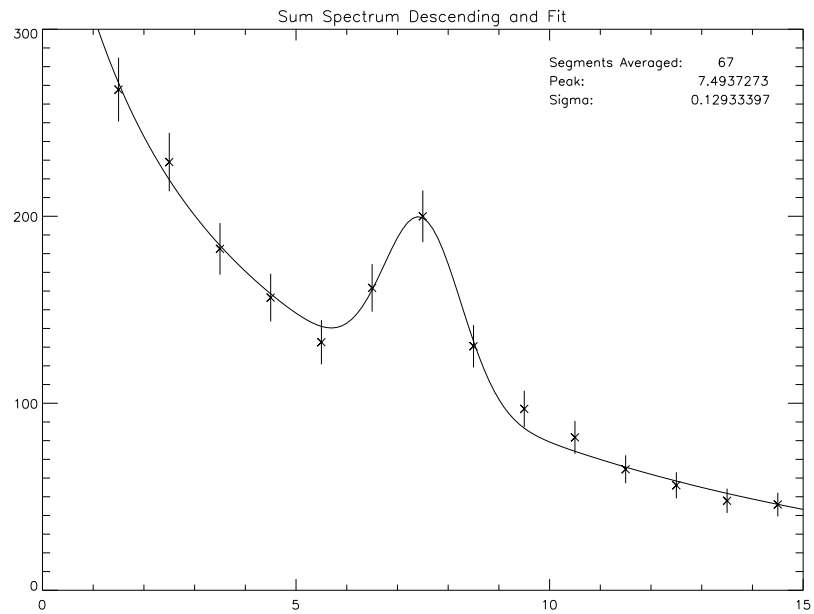

Fig. 24.— The 8 keV line peak observed in layer 1 after the ^{55}Fe feature has been removed. This observation was done during the descending orbit segment.

3.5. DIB Mode 5

In Figures 26-30 we show fits to the $^{55}_{26}$Fe line observed during calibration observations in DIB mode 5. Figure 26 shows the summation of a number of mode 5 calibration observations while USA was in darkness on the descending segment of the ARGOS orbit. Both the main $^{55}_{26}$Fe peak and the escape peak are clearly present in the data. Furthermore, notice that the background, which is modeled in this fit with a third order polynomial, is well behaved down to very low energies. A third line appears to be present above the Fe-main peak but its energy is not consistent with the interpretation of a fluorescence line. An important complexity of this data set is presented in Figure 29. There we show the change in the mean fitted channel for the main $^{55}_{26}$Fe peak during lifetime of the USA mission during the descending orbit segments. The time axis is days after January 1, 1999 at 00:00:00 UTC. Inspection of the plot show that the derived main peak centroid has drifted by one channel from the beginning to the end of the mission.

On the sun-lite (ascending orbit segments) side of the USA orbit the situation is significantly more complex still. In Figures 27, and 28 we show fits to sun-lite calibration $^{55}_{26}$Fe observations in DIB mode 5. Notice that the low energy background counts are not nearly so well behaved as on the dark side of the orbit in Figure 28. We attribute this raised count rate to solar X-rays scattered into the USA collimator by residual

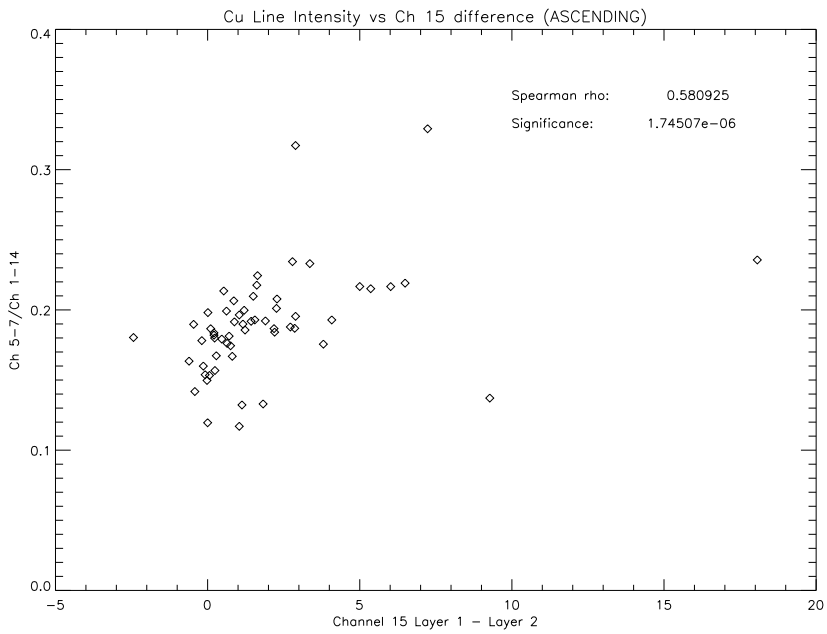

Fig. 25.— The possible correlation of copper fluorescence X-rays with soft electrons.

Earth-atmospheric gas near the height of the ARGOS orbit. Such an effect has been observed in a number of X-ray orbiting experiments such as the Einstein Observatory IPC (Fink, Schmitt, & Harnden 1988) and ROSAT (Snowden & Freyberg 1993). This makes background estimations in the line fits very difficult and in particular the escape peak is swamped in these and other AN calibration observations. Another unfortunate effect of being in the sunlight is that the centroid of the main Fe peak can be shifted. Notice that in Figure 27 the line centroid is at channel ~ 21.92, roughly consistent with the DN observations. But, in Figure 28 the line has shifted to a higher channel number at ~ 25.51. The full impact of this effect can be seen in Figure 29 where we display the fitted main peak centroids vs. time. Note that there appear to be two different gain curves separated by approximately 3 channels for the ascending orbit segment observations. We speculate that it may be related to when in the sun-lite side of the orbit the calibration was performed. If the calibration was performed relatively early after USA emerged into the sunlight then thermal gradients may not have had time enough to develop and shift the line as described in Appendix 8. On the other hand, if the observation was done after USA had been warming for several minutes then thermal gradients could have shifted the line significantly. We are investigating why this shift occurs. Linear fits to the drift with time of the ${}^{55}_{26}$Fe and an *assumed* drift in the escape peak give the drift with time represented in Equations 4 and 5.

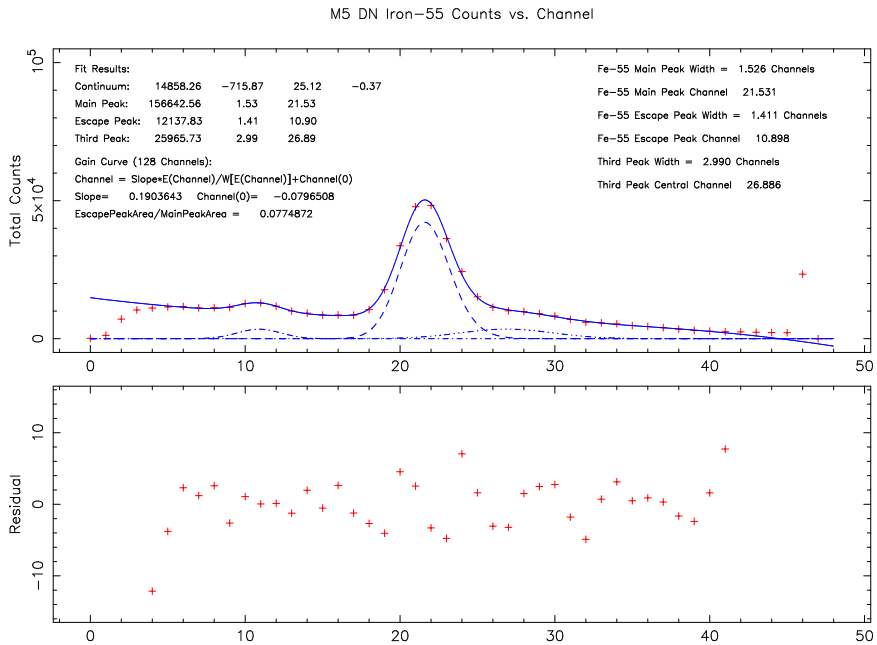

Fig. 26.— The DIB science mode 5 descending orbit segment ^{55}Fe calibration line fit. The fit to the double-gaussian for the main peak and the single gaussian for the escape peak is good. Also, the background counts are well behaved at low energies.

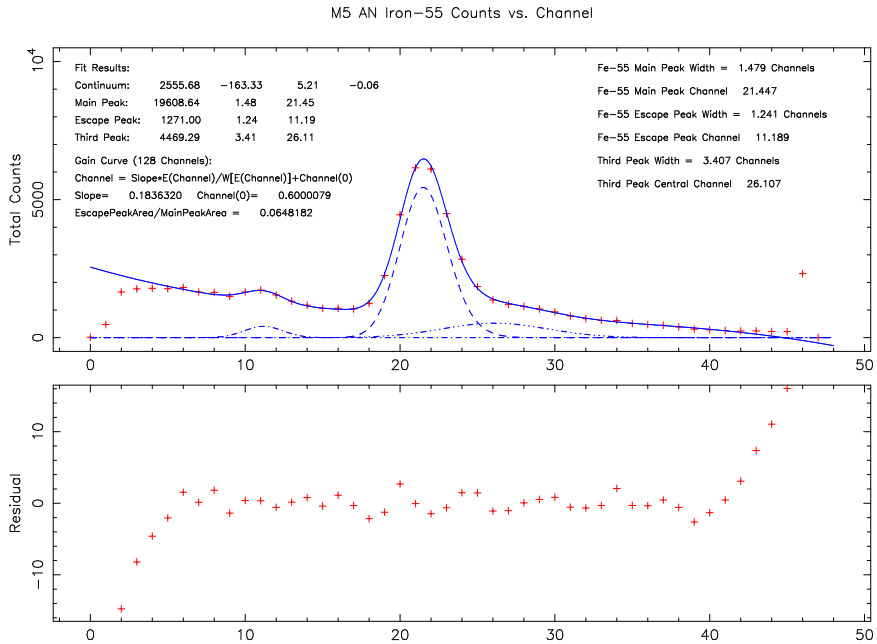

Fig. 27.— The DIB science mode 5 ascending orbit segment ^{55}Fe calibration line fit. The fit to the double-gaussian for the main peak and the single gaussian for the escape peak is good. Also, the background counts are well behaved at low energies for this data set.

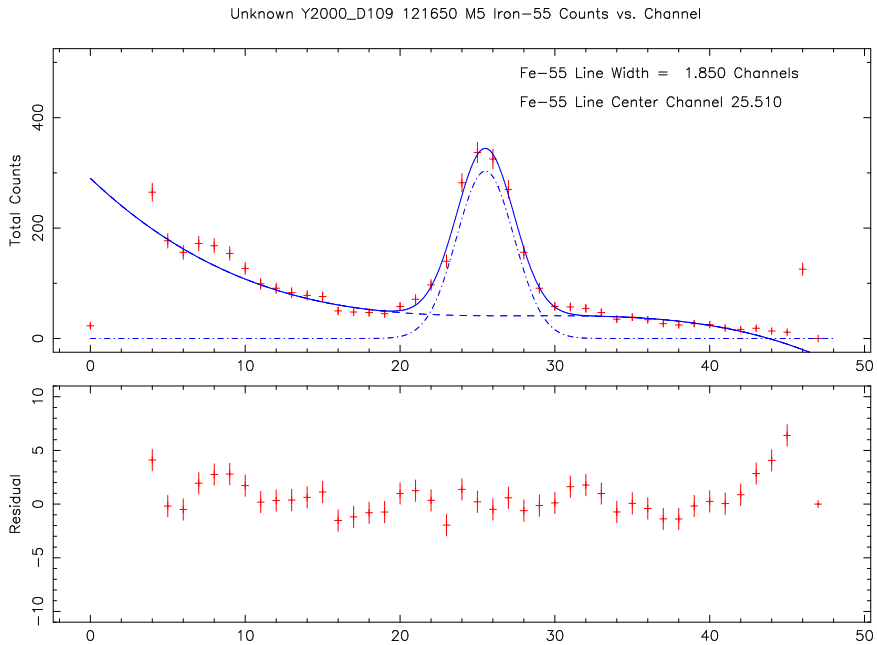

Fig. 28.— Fe Calibration Peak: DIB Mode 5 ascending orbit node. Note that the centroid of the iron line fit is now shifted by several channels.

Ascending	*Offset*	*Linear*	*Quadratic*
Layer 1	1.6430E-1	1.1359E-1	0.0
Layer 2	4.0176E-2	1.2089E-1	0.0
Descending			
Layer 1	4.798E-1	1.260E-1	0.0
Layer 2	4.2686E-2	1.2445E-1	0.0

Table 5: Gain parameters: Energy (keV) to Channel (128) fit (in orbit) for DIB Modes 1 through 4.

Ascending	*Offset*	*Linear*	*Quadratic*
Layer 12	1.11927E-1	1.17604E-1	0.0
Descending			
Layer 12	-7.6757E-2	1.38460E-1	0.0

Table 6: Gain parameters: Energy (keV) to Channel (128) fit (in orbit) for DIB Mode 5.

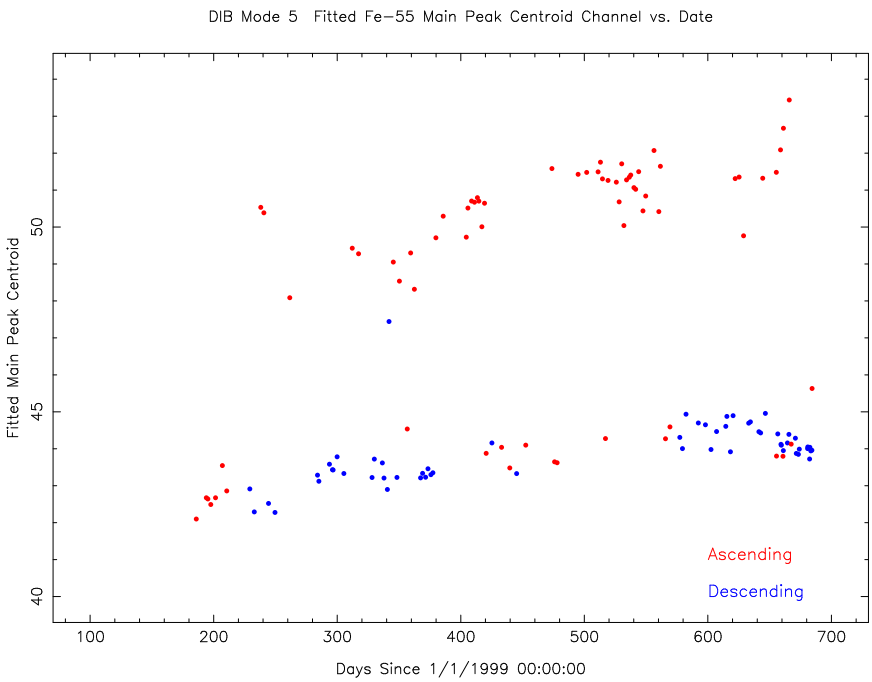

Fig. 29.— The drift of the ^{55}Fe main calibration peak fitted channel centroid with time for the duration of the USA mission. The blue (red) dots represent data is taken during descending (ascending) orbit segment. The channel values are now in raw PHA values (128 channels) rather than the DIB-based 48 channel mode 5 values. The centroid of the ^{55}Fe fit slowly shifts by two channels during the USA lifetime for the descending orbit peaks and by close to four channels for some of the ascending orbit peaks. Note also that there are two distributions of points for the ascending orbit segments. For the ascending orbit segments data there appear to be two different gain curves.

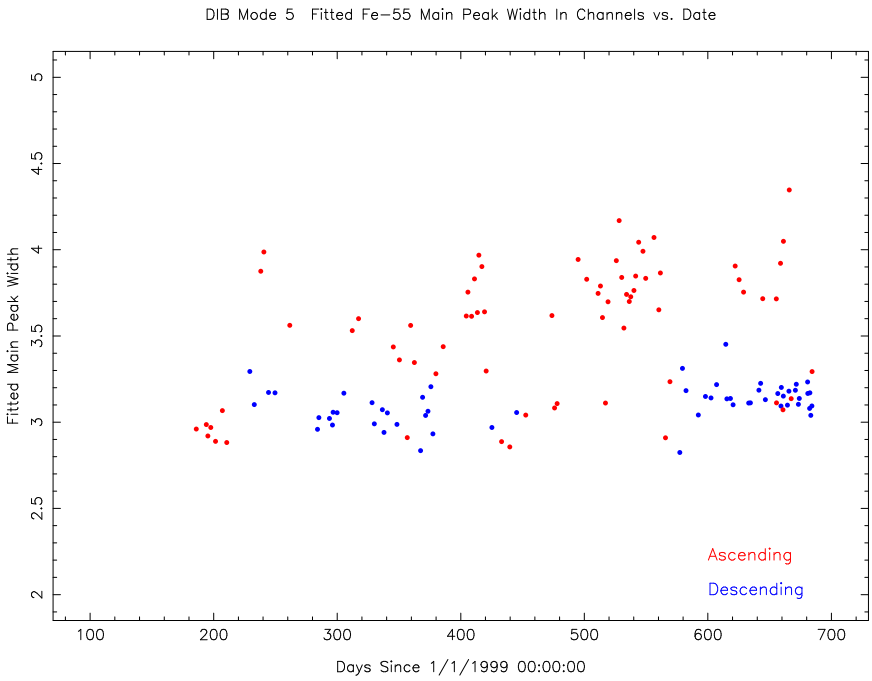

Fig. 30.— The drift of the ^{55}Fe main calibration peak fitted width with time for the duration of the USA mission. The blue (red) dots represent data is taken during descending (ascending) orbit segment. The channel values are now in raw PHA values (128 channels) rather than the DIB-based 48 channel mode 5 values.

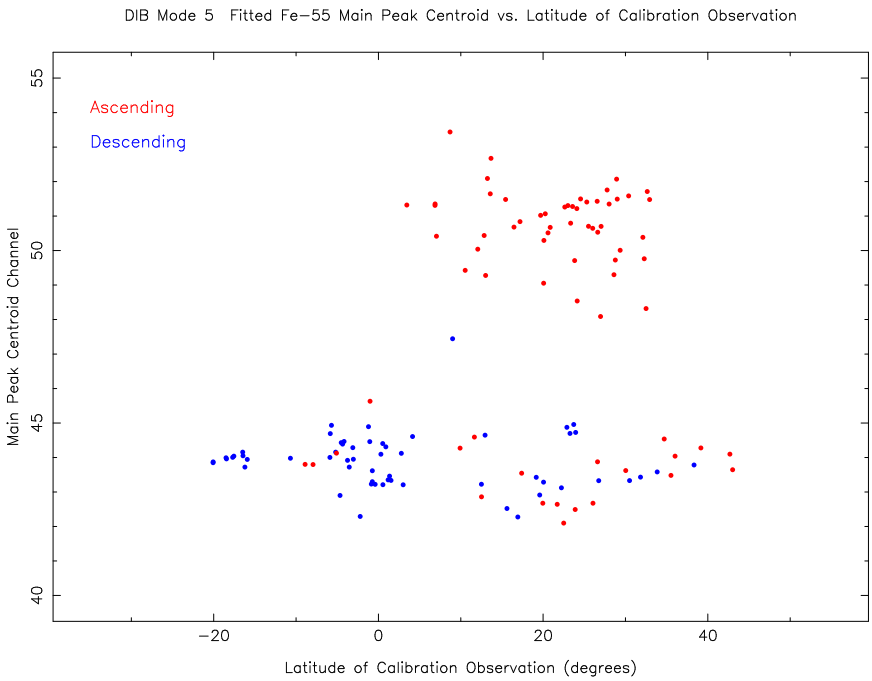

Fig. 31.— The value of the mean latitude of the calibration observations vs. the ^{55}Fe main calibration peak fitted centroid for the duration of the USA mission. The blue (red) dots represent data is taken during descending (ascending) orbit segment. The channel values are now in raw PHA values (128 channels) rather than the DIB-based 48 channel mode 5 values. There does not appear to be a correlation between the fitted peak channel and the latitude of ARGOS during the observation.

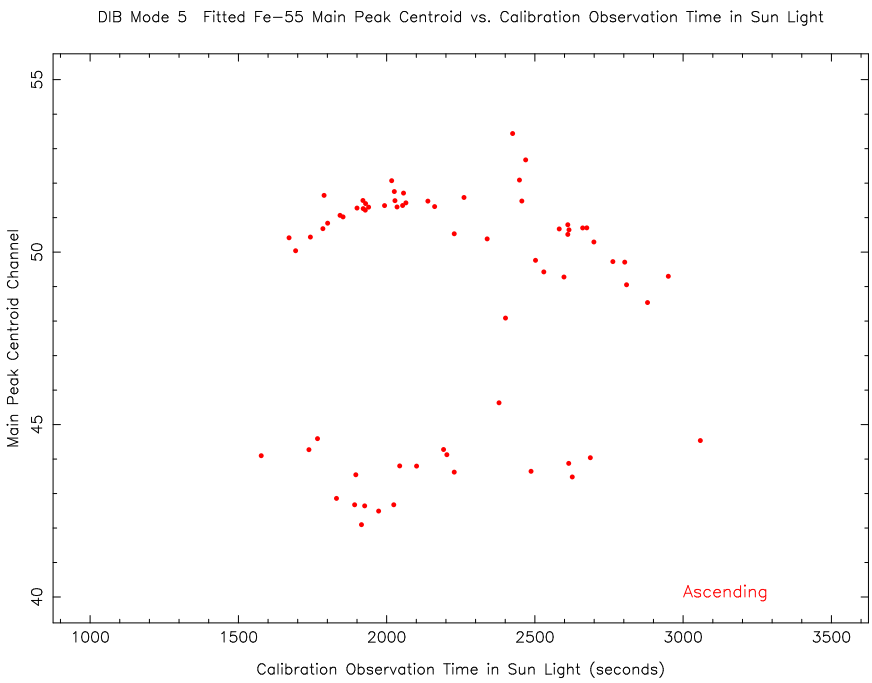

Fig. 32.— The value of the amount of time in sunlight for ARGOS at the time of the calibration observations vs. the ^{55}Fe main calibration peak fitted centroid for the duration of the USA mission. The blue (red) dots represent data is taken during descending (ascending) orbit segment. The channel values are now in raw PHA values (128 channels) rather than the DIB-based 48 channel mode 5 values.

4. USA Response Matrices

The response matrix is a Flexible Image Transport System (FITS) file which contains arrays describing the characteristic response of USA to incoming X-rays. The response matrices are required by XSPEC (the X-ray spectral fitting software developed by NASA and used to model source spectra) in combination with the observed source spectrum and a background spectrum, to perform spectral modeling. As its name implies, it is a matrix, and it has the form R(i,E), giving the probability that an incoming photon of energy E will be detected in channel i (for more details see George et al. (1992) and Arnaud et al. (1992)). In order to create these matrices, two main aspects of the instrument must be considered as in the previous sections: the energy-to-PHA channel conversion and the detection efficiency as a function of energy. Using the USA calibration sources, all the necessay information can be derived to create a model response as a function of energy that can be expressed in the response file format. Three computer codes must be executed in order to build a FITS format response file suitable for inclusion in the spectral modeling process.

4.1. USA Response Matrix Generation Programs

All the programs needed to create USA response matrices are listed in Table 7 and are part of the USA data analysis software library. The computer code "usaarf" is used to create the "Ancillary Response Matrix File". This FITS formated file has the suffix ".arf" and contains all the information required to model the USA detector characteristics resulting from considerations of effective area, window or other USA component transmissions, and detector gas efficiency. The code "usarmf" is used to create the "Redistribution Response Matrix File". This FITS formated file has the suffix ".rmf" and contains all the information required to model the USA detector characteristics resulting from considerations of energy redistribution such as escape peaks, energy resolution, partial charge collection, the the energy-to-PHA channel conversion. A USA "Response Matrix File" having the suffix ".rsp" is created by simply multiplying the .rmf and the .arf matrix files together and can be done with the software tools available in the FTOOLS library. A Perl script ("usarsp") is available to oversee the creation of the response matrix files. Using these tools requires that the environment variable "USA_ROOT_DIR" be set and the directory "$USA_ROOT_DIR/doc/USARefData/" must exist and have all the required files in it. Each of these software tools can be run from the command line on a Unix-based machine that the USA software library is installed on. In order to install and utilize these software tools the standard software distribution LHEASoft must also be installed on the user's computer. LHEASoft is available from the HEASARC web site at URL: http://heasarc.gsfc.nasa.gov/docs/corp/software.html.

Due to the temperature dependent gain variations, a different set of seven response matrices were created for ascending and descending orbit segment observations. Thus, there are a total of 14 different response matrices that the user could generate for various observations. As of January 2004 these computer codes do not contain algorithms to compensate for the gain drifts shown in Figures 29 and 30. Furthermore, we still must develope method for compensating for the split-nature of the ascending orbit segment gain curves. Later releases of the USA response software should contain algorithms meant to account for these drifts.

4.2. USA Data Modes & Response Matrix Files

The data gathered from USA observations is processed by the Detector Interface Board (DIB), which transmits it to the spacecraft interface. The DIB formats the data by determining how many bits will be used to store specific information about the events detected. Five different science modes were programmed

Code Name	Language	Function	Comments
usaarf	C	Create .arf files	Contains information about USA effective area and transmission vs. energy. Help message available.
usarmf	C	Create .rmf files	Contains information about redistribution of photon energies, energy resolution, and energy vs. PHA channel. Help message available.
usarsp	Perl	Script to generate .rsp files.	Calls usarmf and usaarf. Only code the user needs to work with. Help message available.

Table 7: USA response matrix computer codes

Filename	Modes	Layers	Number of channels	Orbit Segment
usad1m1l1dn.rsp	1 and 2	1	16	Descending
usad1m1l2dn.rsp	1 and 2	2	16	Descending
usad1m3l1dn.rsp	3 and 4	1	8	Descending
usad1m3l2dn.rsp	3 and 4	2	8	Descending
usad1m1l12dn.rsp	1 and 2	1 and 2	16	Descending
usad1m3l12dn.rsp	3 and 4	1 and 2	8	Descending
usad1m5l12dn.rsp	5	1 and 2	47	Descending
usad1m1l1an.rsp	1 and 2	1	16	Ascending
usad1m1l2an.rsp	1 and 2	2	16	Ascending
usad1m3l1an.rsp	3 and 4	1	8	Ascending
usad1m3l2an.rsp	3 and 4	2	8	Ascending
usad1m1l12an.rsp	1 and 2	1 and 2	16	Ascending
usad1m3l12an.rsp	3 and 4	1 and 2	8	Ascending
usad1m5l12an.rsp	5	1 and 2	47	Ascending

Table 8: USA response matrices

into the DIB. These modes are summarized in Table 9.

Raw photon event data is binned in one of 128 "raw" PHA modes early in the event processing. However, this raw channel binning information is not contained in the data telemetred to the ground because the PHA information is rebinned into a smaller set of spectral bins depending on which of the 5 USA "Science Data Modes" ("DIB mode"; summarized in Table 9) the observation is performed in. The DIB modes can be summarized as follows: 4 "timing" modes (DIB modes 1 through 4) and a "spectral" mode (DIB mode 5). DIB modes 1 and 2 have 16 channels, 8 PHA channels combined into each 1 final channel. Modes 3 and 4 have only final 8 channels, so each of these channels corresponds to 16 of the original PHA channels. Mode 5 is a binned spectral mode. One PHA spectrum is taken every 10 milliseconds with no information is retained on individual events. This mode divides the PHA spectrum into 48 channels. However, rather than being binned linearly, it is binned more heavily at low energies. The first 30 channels correspond to the first 60 PHA channels while the next 17 channels are obtained by linearly rebinning the final 68 PHA channels. A channel with 0 response is tacked onto the DIB mode 5 spectra at the end. This sort of spectral binning allows for finer resolution at lower energies where more counts are expected.

The different "timing" modes are distinguished not only by their timing and spectral resolution, but also by their telemetry rate. The "low" telemetry timing modes (at 40 kbps) begin to fill the buffer at rates of just over 1000 counts per second and are therefore not well suited for bright sources (many events would be lost in every frame). Of the two high-telemetry modes, mode 2 was the most widely used, sacrificing some time resolution (32 μs vs 2 μs for mode 3) in favor of better spectral resolution (16 channels vs 8 for mode 3). We show the derived descending orbit node channels and energies in Appendix 9 based on our DIB mode 5 calibration observations while on-orbit. See Shabad (2000) for more details on USA observing modes, their uses and limitations.

Mode	Name	Time Resolution	# Channels	Telemetry Rate (kbps)
1	Normal Low Rate Event Mode	32 μs	16	40
2	Normal High Rate Event Mode	32 μs	16	128
3	Alternate Low Rate Event Mode	2 μs	8	40
4	Alternate High Rate Event Mode	2 μs	8	128
5	Spectral	10 ms	48	40

Table 9: USA science observing modes.

4.3. Fitting the Crab Energy Spectrum

The Crab Nebula represents a standard X-ray source which has been used for calibrating most X-ray telescopes for the last 30 years. The X-ray emission from the diffuse region of the Crab appears to be constant, to within 10% (Willingale et al. 2001). Toor & Seward (1974) used 28 different spectra obtained from rocket and balloon experiments to derive an absolute calibration for the Crab to within 10%. The spectral fit parameters they obtained between 2 and 60 keV are:

$$I(E) = 9.7 \pm 1.0 E^{-2.10 \pm 0.03} \text{ photons/cm}^2\text{/sec/keV} \tag{19}$$

The value for the galactic absorption in units of the equivalent hydrogen column density is $n_H = 0.33 \times 10^{22}$ atoms cm^{-2}.

Figure 33 shows a typical fit (in the 2–14 keV range) to the Crab energy spectrum (this particular observation was in the descending node). For a background estimation we used the USA background estimation tool *"usabckgnd"*. For DIB mode 2 data we used an absorbed power law as the model, adding a gaussian to model the copper fluorescence line which shows up at around 8 keV. We obtain a power-law photon index of 2.159 ± 0.006 consistent with the accepted value of 2.1 Toor & Seward. The flux we obtain for the Crab in the 2–10 keV region is 2.9×10^{-8}erg cm^{-2} s^{-1}, which also agrees with previous observations. Table 10 summarizes the results of the test fits we performed for USA Crab observations.

For DIB mode 5 data we also used an absorbed power law as the model, but did not add a copper fluorescence line. Results for this fit are shown in Figures 34 and 35. The fit is close to the canonical Crab spectral parameters. We show two fits, the first fit ignoring energy channels outside the range 1.29-16.15 keV and the second fit ignoring energy channels outside the range 1.78-16.15 keV. For the first fit we obtain a photon power-law index of 2.1089 ± 0.0059, very close to the accepted value of 2.1 Toor & Seward. Furthermore, we find that XSPEC makes the interstellar hydrogen absorption column density

Obs ID	Spectral Index	Normalization	Column Density	Reduced χ^2	Channels
Y1999 D323 223553	2.0444±0.0050	7.27±0.06	0.149±0.007	2.337	1-14
Y1999 D324 052102	2.0316±0.0050	7.27±0.06	0.150±0.007	2.093	1-14
Y1999 D324 070418	2.0382±0.0070	7.67±0.08	0.136±0.010	2.076	1-14
Y1999 D325 101711	2.0812±0.0054	6.78±0.06	0.148±0.008	2.739	1-14
Y1999 D325 133719	2.0502±0.0051	7.06±0.06	0.144±0.007	1.890	1-14
Y1999 D330 120650	2.0111±0.0048	7.68±0.06	0.121±0.007	2.700	1-14
Y1999 D331 114933	2.0323±0.0048	7.96±0.06	0.145±0.007	1.500	1-14
Y1999 D332 131533	2.0357±0.0049	7.68±0.06	0.151±0.007	2.094	1-14
Y1999 D333 143954	2.0587±0.0052	7.29±0.06	0.146±0.007	1.127	1-14
Y1999 D334 142237	2.0535±0.0052	7.16±0.06	0.169±0.008	1.158	1-14
Y1999 D335 122202	2.0237±0.0048	7.93±0.06	0.138±0.007	1.699	1-14
Y1999 D337 114727	2.0120±0.0047	8.02±0.06	0.141±0.007	3.303	1-14
Y1999 D341 223611	2.0963±0.0051	7.17±0.06	0.109±0.007	1.427	1-14
Y1999 D342 120729	2.0599±0.0049	7.43±0.06	0.157±0.007	1.814	1-14
Y1999 D343 114651	2.0462±0.0049	7.52±0.06	0.155±0.007	1.195	1-14
Y1999 D344 080447	1.9918±0.0051	6.61±0.05	0.126±0.007	3.015	1-14
Y1999 D346 073011	2.0148±0.0050	6.98±0.05	0.160±0.007	2.059	1-14
Y2000 D290 142547	2.0314±0.0048	6.69±0.05	0.184±0.007	2.889	1-14
Y2000 D310 202828	2.0309±0.0049	6.67±0.05	0.181±0.007	1.935	1-14
Y2000 D311 013218	2.0297±0.0049	6.59±0.05	0.188±0.007	2.216	1-14

Table 10: USA DIB Mode 2 Descending Crab calibration fit results. Both layers are included in the fits, a systematic error of 2% is added to all errors in the XSPEC fits, and only energies in the range 1-16 keV are included.

$n_H = 0.264 \pm 0.080 \times 10^{22}$ atoms/cm^2. The normalization on the spectrum, however, is 7.609 ± 0.068, somewhat lower than the accepted value. This fit is obtained with a χ^2 value of 8.151 with 37 degrees of freedom.

For the second energy range fit we obtain a photon power-law index of 2.0742 ± 0.0077, again very close to the accepted value of 2.1 Toor & Seward. Furthermore, we find that XSPEC makes the interstellar hydrogen absorption column density $n_H = 0.157 \pm 0.017 \times 10^{22}$ atoms/cm^2. The normalization on the spectrum, however, is 7.14 ± 0.09, somewhat lower than the accepted value. This fit is obtained with a χ^2 value of 7.199 with 35 degrees of freedom.

5. Conclusions

An energy calibration of USA was carried out with 1996 ground data, which provided the highest resolution (128 channels). This calibration was then checked and improved with calibration data taken in orbit. A different energy gain curve is required for ascending and descending orbit node ("dark" side) observations. The observed differences between the ascending and descending node observations appears to result from a thermal gradient that is present in the detector body once it begins to heat due to solar irradiation. The 1996 ground calibration appears to be consistent with the descending node in-orbit calibration. We checked

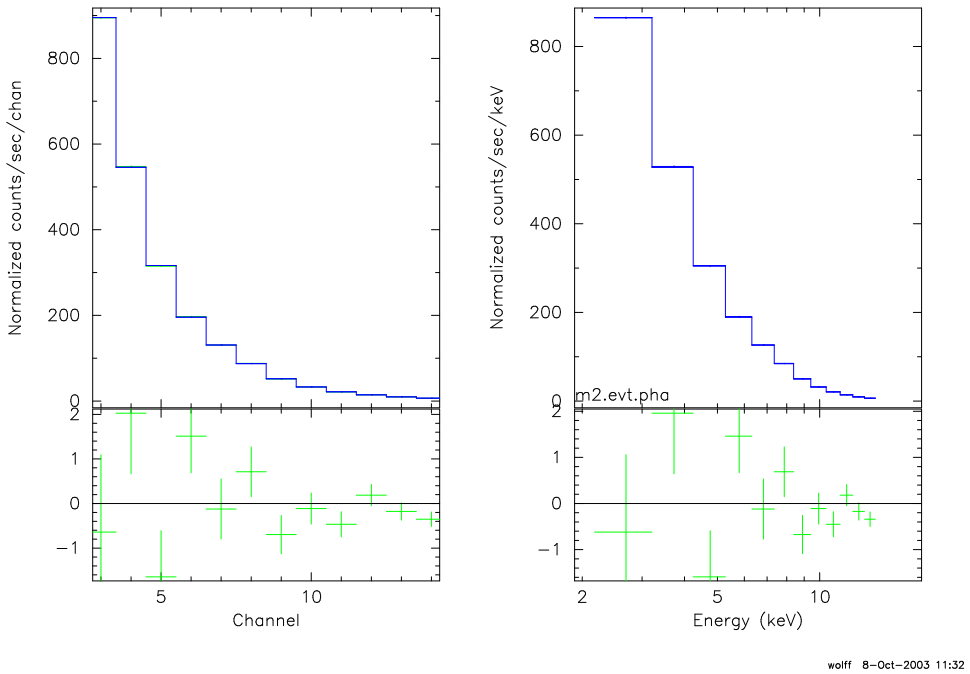

Fig. 33.— Crab spectral fit in DIB Mode 2 and including counts from both layers. This observations was obtained as ARGOS was in the descending part of its orbit.

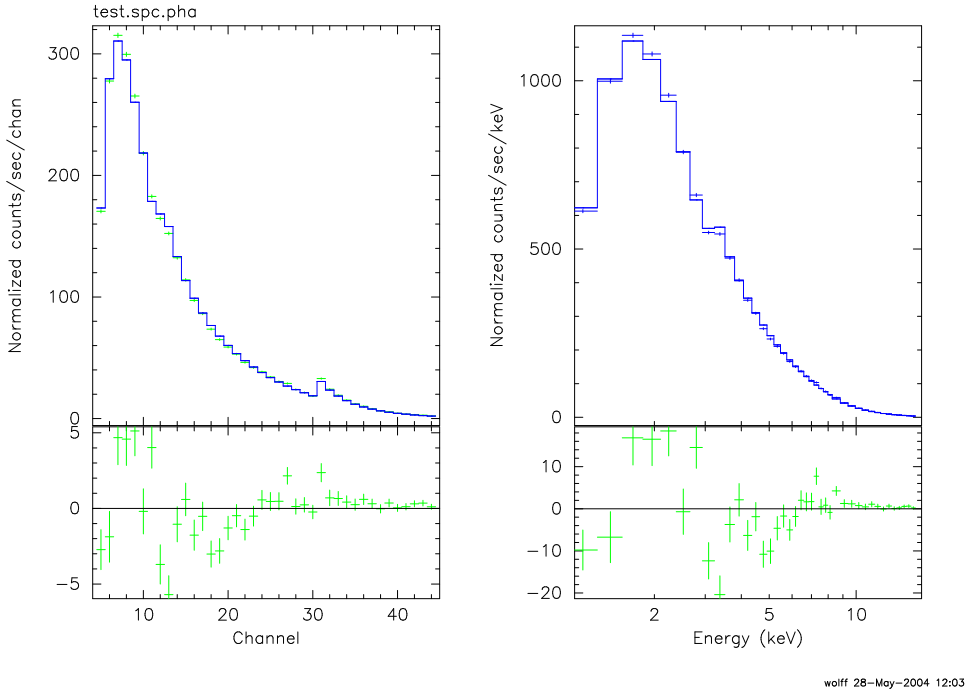

Fig. 34.— Crab spectral fit in DIB Mode 5. This observations was obtained as ARGOS was in the descending part of its orbit. The observation is Y1999 D334 055250 shown in Tables 14 and 15. The fitted energy range is 0.97-16.1 keV.

Obs ID	Spectral Index	Normalization	Column Density	Reduced χ^2	Channels
Y1999 D323 223553	1.9914±0.0087	6.50±0.10	0.000±0.000	3.348	2-14
Y1999 D324 052102	1.9674±0.0088	6.36±0.10	0.000±0.000	3.722	2-14
Y1999 D324 070418	1.9884±0.0121	6.96±0.15	0.000±0.000	2.712	2-14
Y1999 D325 101711	2.0603±0.0096	6.51±0.11	0.048±0.038	3.324	2-14
Y1999 D325 133719	2.0136±0.0089	6.52±0.11	0.000±0.000	2.268	2-14
Y1999 D330 120650	1.9649±0.0084	6.97±0.11	0.000±0.000	2.266	2-14
Y1999 D331 114933	2.0020±0.0083	7.44±0.11	0.000±0.000	1.637	2-14
Y1999 D332 131533	2.0019±0.0086	7.15±0.11	0.000±0.000	2.348	2-14
Y1999 D333 143954	2.0225±0.0090	6.78±0.11	0.000±0.000	1.396	2-14
Y1999 D334 142237	2.0158±0.0091	6.64±0.11	0.000±0.000	1.283	2-14
Y1999 D335 122202	1.9847±0.0083	7.28±0.11	0.000±0.000	1.552	2-14
Y1999 D337 114727	1.9547±0.0082	7.13±0.11	0.000±0.000	2.398	2-14
Y1999 D341 223611	2.0807±0.0090	6.95±0.11	0.034±0.036	1.645	2-14
Y1999 D342 120729	2.0284±0.0087	6.95±0.11	0.000±0.000	2.090	2-14
Y1999 D343 114651	2.0002±0.0085	6.82±0.11	0.000±0.000	1.567	2-14
Y1999 D344 080447	1.9401±0.0088	5.95±0.10	0.000±0.000	2.538	2-14
Y1999 D346 073011	1.9560±0.0088	6.17±0.10	0.000±0.000	2.572	2-14
Y2000 D290 142547	1.9505±0.0082	5.65±0.08	0.000±0.000	3.433	2-14
Y2000 D310 202828	1.9783±0.0083	5.96±0.09	0.000±0.000	1.654	2-14
Y2000 D311 013218	1.9419±0.0084	5.50±0.08	0.000±0.000	2.690	2-14

Table 11: USA DIB Mode 2 Descending Crab calibration fit results. Both layers are included in the fits, a systematic error of 2% is added to all errors in the XSPEC fits, and only energies in the range 2-16 keV are included.

the energy calibration with 1997 and 1998 TVAC data and found that at times these data seemed to be consistent with the ascending node in-orbit calibration while at other times it was more consistent with the descending node calibration. The source of such discrepancies is not certain, but as a result, the 1997 and 1998 ground calibration data were not used to build the USA response matrices. The current USA response matrices were built using mainly in-orbit data. The peak of the iron calibration source as well as the observed copper fluorescence peak were used to produce a linear fit for the gain in both ascending and descending node observations. Using these fits and the USA efficiencies, two sets of response matrices were created, one for each of the ascending and descending sides of the orbit. Finally, these response matrices were tested in XSPEC to fit the Crab energy spectrum with an absorbed power law, yielding a power-law index and flux which agrees with past observations for DIB mode 2 observations. For DIB mode 5 Crab spectral observations the fits are not as consistent with the canonical Crab power law and interstellar absorption values. We hope to address the deficiency in later releases of the USA response matrices. We have developed computer codes for the generation of USA response matrices. This greatly simplifies the task of generating new response functions for use with the FTOOLS XSPEC when the need arises.

In the near future we hope to address the following still outstanding issues.

1. We will develop software algorithms to compensate for the gain drifts with time for both teh ascending and descending orbit segment observations. 2. We hope to do a better job of accounting for source self-veto events in the response matrices. 3. Does the actual Crab power law spectrum soften at low energies such

Obs ID	Spectral Index	Normalization	Column Density	Reduced χ^2	Channels
Y1999 D323 223553	2.1519±0.0062	8.82±0.08	0.278±0.009	5.432	1-14
Y1999 D324 052102	2.1172±0.0061	8.56±0.08	0.249±0.009	5.116	1-14
Y1999 D324 070418	2.1393±0.0085	9.24±0.12	0.258±0.012	3.529	1-14
Y1999 D325 101711	2.1791±0.0066	8.15±0.08	0.269±0.009	6.669	1-14
Y1999 D325 133719	2.1627±0.0062	8.66±0.08	0.287±0.009	3.605	1-14
Y1999 D330 120650	2.0905±0.0058	8.95±0.08	0.211±0.008	4.799	1-14
Y1999 D331 114933	2.1224±0.0058	9.47±0.08	0.251±0.008	4.161	1-14
Y1999 D332 131533	2.1445±0.0060	9.37±0.09	0.282±0.009	4.764	1-14
Y1999 D333 143954	2.1509±0.0063	8.67±0.08	0.255±0.009	3.456	1-14
Y1999 D334 142237	2.1446±0.0064	8.51±0.08	0.280±0.009	4.322	1-14
Y1999 D335 122202	2.1136±0.0058	9.39±0.08	0.241±0.008	2.889	1-14
Y1999 D337 114727	2.0930±0.0058	9.44±0.08	0.253±0.008	6.578	1-14
Y1999 D341 223611	2.2257±0.0063	8.97±0.09	0.257±0.009	4.344	1-14
Y1999 D342 120729	2.1648±0.0061	9.01±0.08	0.283±0.009	4.815	1-14
Y1999 D343 114651	2.1364±0.0060	8.91±0.08	0.259±0.009	3.540	1-14
Y1999 D344 080447	2.0648±0.0062	7.67±0.07	0.218±0.009	5.491	1-14
Y1999 D346 073011	2.0946±0.0061	8.15±0.08	0.257±0.009	4.927	1-14
Y2000 D290 142547	2.1227±0.0059	7.90±0.07	0.282±0.008	5.589	1-14
Y2000 D310 202828	2.1235±0.0060	7.89±0.07	0.280±0.008	5.209	1-14
Y2000 D311 013218	2.1143±0.0060	7.71±0.07	0.277±0.008	5.823	1-14

Table 12: USA DIB Mode 2 Descending Crab calibration fit results. Only layer 1 events are included in the fits, a systematic error of 2% is added to all errors in the XSPEC fits, and only energies in the range 1-16 keV are included.

that our estimated model fits are better than we have represented in this report. This is part of a general effort to better understand our low energy (1-3 keV) response than we do at present.

Obs ID	Spectral Index	Normalization	Column Density	Reduced χ^2	Channels
Y1999 D323 223553	2.1050±0.0044	8.02±0.05	0.000±0.000	6.534	2-14
Y1999 D324 052102	2.0866±0.0044	7.97±0.05	0.000±0.000	5.846	2-14
Y1999 D324 070418	1.9989±0.0145	7.04±0.18	0.000±0.000	10.397	2-14
Y1999 D325 101711	2.0813±0.0114	6.75±0.14	0.000±0.000	12.327	2-14
Y1999 D325 133719	2.1118±0.0045	7.82±0.05	0.000±0.000	4.375	2-14
Y1999 D330 120650	2.0519±0.0042	8.30±0.05	0.000±0.000	3.933	2-14
Y1999 D331 114933	2.0915±0.0042	8.80±0.05	0.000±0.000	4.701	2-14
Y1999 D332 131533	2.0974±0.0043	8.51±0.05	0.000±0.000	5.623	2-14
Y1999 D333 143954	2.1062±0.0045	7.91±0.05	0.000±0.000	4.333	2-14
Y1999 D334 142237	2.0957±0.0046	7.71±0.05	0.000±0.000	5.499	2-14
Y1999 D335 122202	2.0803±0.0042	8.72±0.05	0.000±0.000	2.938	2-14
Y1999 D337 114727	2.0467±0.0042	8.59±0.05	0.000±0.000	5.312	2-14
Y1999 D341 223611	2.1643±0.0108	7.97±0.15	0.000±0.000	7.336	2-14
Y1999 D342 120729	2.1141±0.0043	8.13±0.05	0.000±0.000	6.186	2-14
Y1999 D343 114651	2.0040±0.0101	6.86±0.13	0.000±0.000	10.677	2-14
Y1999 D344 080447	2.0226±0.0044	7.07±0.04	0.000±0.000	4.258	2-14
Y1999 D346 073011	2.0580±0.0044	7.53±0.05	0.000±0.000	5.173	2-14
Y2000 D290 142547	2.0888±0.0042	7.30±0.04	0.000±0.000	5.917	2-14
Y2000 D310 202828	2.0894±0.0042	7.29±0.04	0.000±0.000	5.526	2-14
Y2000 D311 013218	2.0803±0.0042	7.13±0.04	0.000±0.000	6.020	2-14

Table 13: USA DIB Mode 2 Descending Crab calibration fit results. Only layer 1 events are included in the fits, a systematic error of 2% is added to all errors in the XSPEC fits, and only energies in the range 2-16 keV are included.

Obs ID	Spectral Index	Normalization	Column Density	Reduced χ^2	Channels
Y1999 D324 221837	2.0791±0.0058	8.66±0.07	0.233±0.007	2.000	5-44
Y1999 D325 220121	2.0715±0.0041	8.23±0.05	0.190±0.005	1.685	5-44
Y1999 D329 071926	2.0299±0.0041	7.58±0.05	0.116±0.005	2.125	5-44
Y1999 D334 055250	2.0647±0.0060	7.69±0.07	0.182±0.008	1.305	5-44
Y1999 D335 140339	2.0768±0.0042	8.09±0.05	0.209±0.005	2.148	5-44
Y1999 D338 062517	2.0656±0.0042	8.03±0.05	0.181±0.005	2.166	5-44
Y1999 D339 060800	2.0563±0.0042	7.67±0.05	0.197±0.005	2.015	5-44
Y2000 D290 023429	2.0835±0.0056	7.55±0.06	0.161±0.007	1.739	5-44
Y2000 D299 151411	2.0758±0.0041	7.02±0.04	0.196±0.005	1.757	5-44
Y2000 D302 160155	2.0796±0.0042	7.01±0.04	0.249±0.005	2.835	5-44
Y2000 D305 183231	2.0816±0.0042	7.01±0.04	0.219±0.005	2.276	5-44
Y2000 D308 210323	2.0469±0.0041	6.88±0.04	0.229±0.005	3.124	5-44
Y2000 D314 141347	2.0112±0.0041	6.54±0.04	0.147±0.005	3.755	5-44
Y2000 D317 150259	2.0861±0.0042	7.08±0.04	0.216±0.005	2.511	5-44
Y2000 D320 155210	2.0802±0.0041	7.13±0.04	0.211±0.005	2.612	5-44

Table 14: USA DIB Mode 5 Descending Crab calibration fit results. Both layers are included in the fits, a systematic error of 2% is added to all errors in the XSPEC fits, and only energies in the range 1-16 keV are included in the fits.

Obs ID	Spectral Index	Normalization	Column Density	Reduced χ^2	Channels
Y1999 D324 221837	2.0295±0.0076	7.93±0.10	0.089±0.016	1.471	7-44
Y1999 D325 220121	2.0259±0.0054	7.58±0.07	0.061±0.011	1.159	7-44
Y1999 D329 071926	2.0110±0.0055	7.29±0.07	0.026±0.012	1.874	7-44
Y1999 D334 055250	2.0276±0.0080	7.20±0.09	0.079±0.017	0.913	7-44
Y1999 D335 140339	2.0280±0.0055	7.42±0.07	0.069±0.012	1.402	7-44
Y1999 D338 062517	2.0267±0.0055	7.49±0.07	0.065±0.012	1.428	7-44
Y1999 D339 060800	2.0211±0.0056	7.19±0.07	0.079±0.012	1.489	7-44
Y2000 D290 023429	2.0429±0.0073	7.02±0.08	0.045±0.015	1.331	7-44
Y2000 D299 151411	2.0374±0.0053	6.57±0.06	0.094±0.011	1.272	7-44
Y2000 D302 160155	2.0272±0.0054	6.40±0.06	0.108±0.011	1.838	7-44
Y2000 D305 183231	2.0359±0.0054	6.47±0.06	0.097±0.011	1.635	7-44
Y2000 D308 210323	2.0182±0.0053	6.48±0.06	0.102±0.011	2.480	7-44
Y2000 D314 141347	1.9739±0.0054	6.08±0.05	0.024±0.011	2.805	7-44
Y2000 D317 150259	2.0352±0.0054	6.47±0.06	0.072±0.011	1.631	7-44
Y2000 D320 155210	2.0361±0.0053	6.60±0.06	0.091±0.011	1.710	7-44

Table 15: USA DIB Mode 5 Descending Crab calibration fit results. Both layers are included in the fits, a systematic error of 2% is added to all errors in the XSPEC fits, and only energies in the range 1.7-16 keV are included in the fits.

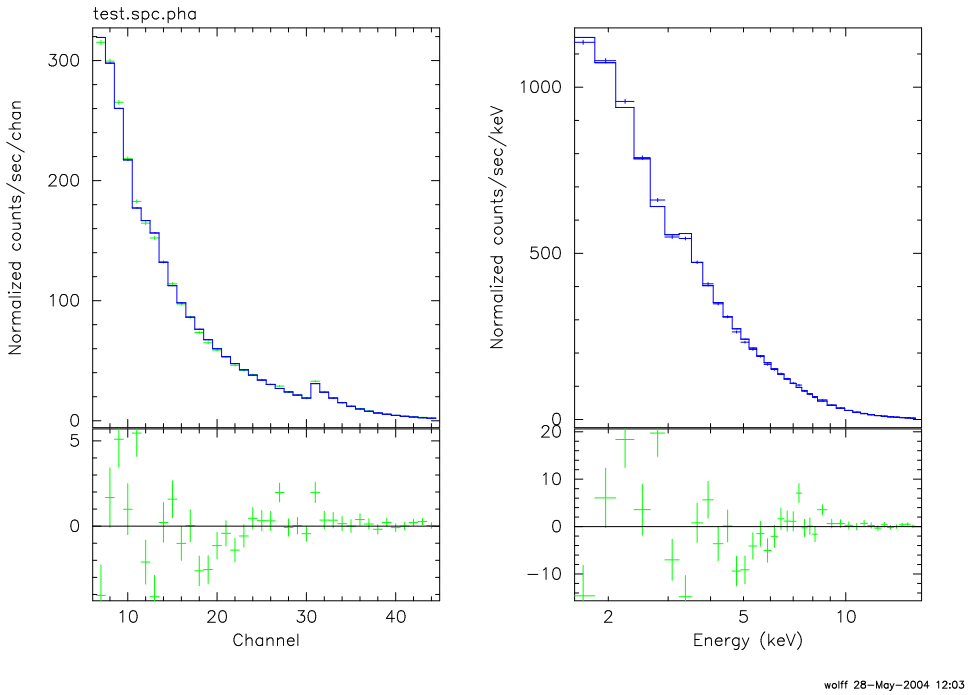

Fig. 35.— Crab spectral fit in DIB Mode 5. This observations was obtained as ARGOS was in the descending part of its orbit. The observation is Y1999 D334 055250 shown in Tables 14 and 15. The fitted energy range is 1.76-16.1 keV.

6. Appendix: The Amplitude of the Argon-Induced Escape Peak

If an escape peak photon K_α or K_β is produced everything depends on whether or not this photon can escape the chamber. If the $K_{\alpha\beta}$ interacts with the P-10 gas before leaving the chamber this affects whether or not an escape peak energy is recorded for the incoming photon or even if that photon is registered at all by the USA DIB. If the $K_{\alpha\beta}$ causes further ionization in the P-10 gas, and that ionization leads to a pulse on a wire other than the wire on which the the original photopeak pulse is registered, the $K_{\alpha\beta}$ photon causes a veto of the original photon and nothing is recorded except a veto event. If, on the other hand, the $K_{\alpha\beta}$ photon interacts with the P-10 producing a pulse on the same wire as the original photopeak pulse then USA will likely record a photon at the original X-ray photon energy. If, finally, and this is our main concern here in this appendix, the $K_{\alpha\beta}$ photon escapes from the chamber entirely then an escape peak event is recorded by the USA DIB.

The probability of interaction $P_i(z, E_\gamma)$ with the P-10 gas by the original X-ray photon at a depth z inside the USA wire chamber is given by a slightly modified form of Equation 10:

$$P_i(z, E_\gamma) \ = 1 - \exp\left[- \left(\frac{\mu}{\rho}\right)_{Ar} (E_\gamma)\ \rho(Ar)\ w(Ar)\ z\ - \left(\frac{\mu}{\rho}\right)_{CH_4} (E_\gamma)\ \rho(CH_4)\ w(CH_4)\ z \right] \tag{20}$$

The probability that this interaction produces an Argon $K_{\alpha\beta}$ photon is simply the fluorescence yield of Argon which is $\omega_F = 0.122$ (Bambynek et al. 1972). Finally, the probability that the $K_{\alpha\beta}$ photon escapes from the chamber can be easily calculated as long as we make a few assumptions. First, we assume that hitting the chamber walls is the same as escaping since few if any photoelectric electrons will be produced. Second, we assume that the chamber can be approximated by a semi-infinite lateral extent, in other words that the chamber is infinite in the directions perpendicular to the z-direction which is the original photon's direction of motion. With these assumptions we can write the probability of escape as the sum of an integration over all upward directions and an integration over all downward directions:

$$P_{es}(z, E(K_{\alpha\beta})) \ = \ \frac{1}{4\pi} \int_0^{2\pi} \int_0^{\pi/2} e^{-\rho z \sigma_A [E(K_{\alpha\beta})]/cos\theta} sin\theta d\theta d\phi \ + \ \frac{1}{4\pi} \int_0^{2\pi} \int_{\pi/2}^{2\pi} e^{\rho(H-z)\sigma_A [E(K_{\alpha\beta})]/cos\theta} sin\theta d\theta d\phi \tag{21}$$

Here, H is the depth of the USA wire chamber as sensed by a photon that emerges into the chamber through the mylar window. The expression $e^{-\rho z \sigma_A [E(K_{\alpha\beta})]}$ is short-hand for the full expression inside the exponential function in Equation 20. The $K_{\alpha\beta}$ photon is assumed to be emitted in a isotropic fashion from the Ar^+ ion. The first integral represents the probability of escape of an upward traveling photon and the second integral represents the escape probability of a downward traveling photon. Thus, the total probability that an incoming photon of energy E_γ will produce an escape peak pulse is then

$$P_T(E_\gamma) \ = \ \int_0^H P_i[z, E_\gamma] \times \ \omega_F \ \times \ P_{es}[z, E(K_\alpha)]\, dz \tag{22}$$

Using the nominal values for the USA detector and P-10 gas cited earlier in this report, a 20-point integration by Gaussian-Legendre Quadrature results in the main photopeak and escape peak amplitudes as shown in Figure 36. The resulting ratio of the main to escape peak amplitudes as a function of energy is shown in Figure 37. According to this analysis the escape peak amplitude varies in size relative to the main peak above the Argon K-edge energy. We include this effect in the calculation of the expected USA response when we compute the response matrices.

If we write that the main peak amplitude is A_m and the escape peak amplitude is A_e and that the ratio

of A_e to A_m is r_{em} then,

$$A_m = \frac{1}{1 + r_{em}}, \tag{23}$$

and,

$$A_e = \frac{r_{em}}{1 + r_{em}}, \tag{24}$$

Calculating the ration of the escape peak to main peak normalization allows the adjustment of the relative normalizations of the main and escape peaks as a function of energy.

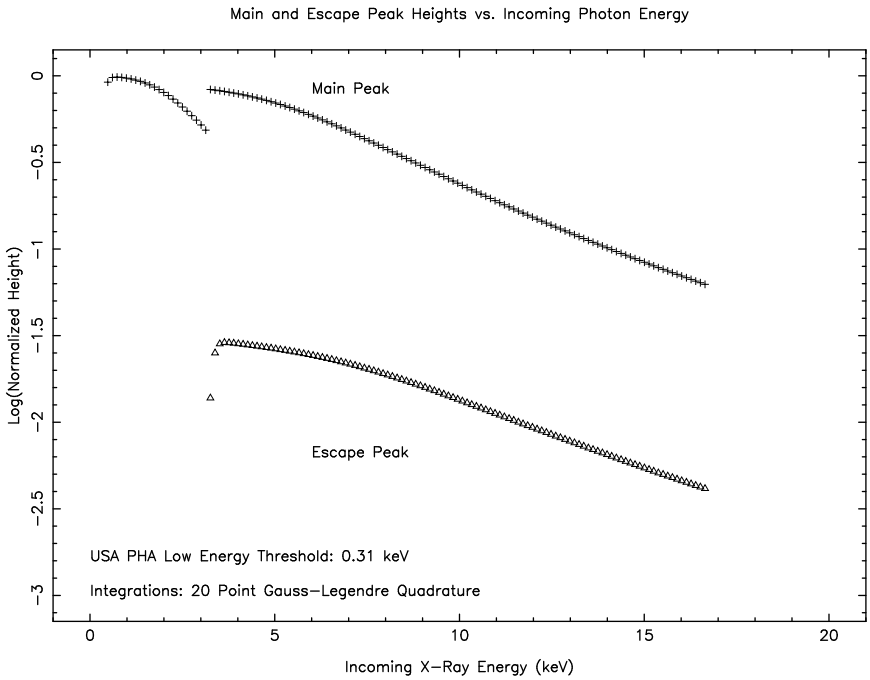

Fig. 36.— The amplitudes of the main and escape peaks as a function of energy for the USA proportional counter chamber in the range 1-15 keV. There is no escape peak at energies below the Argon K-edge at 3.2029 keV.

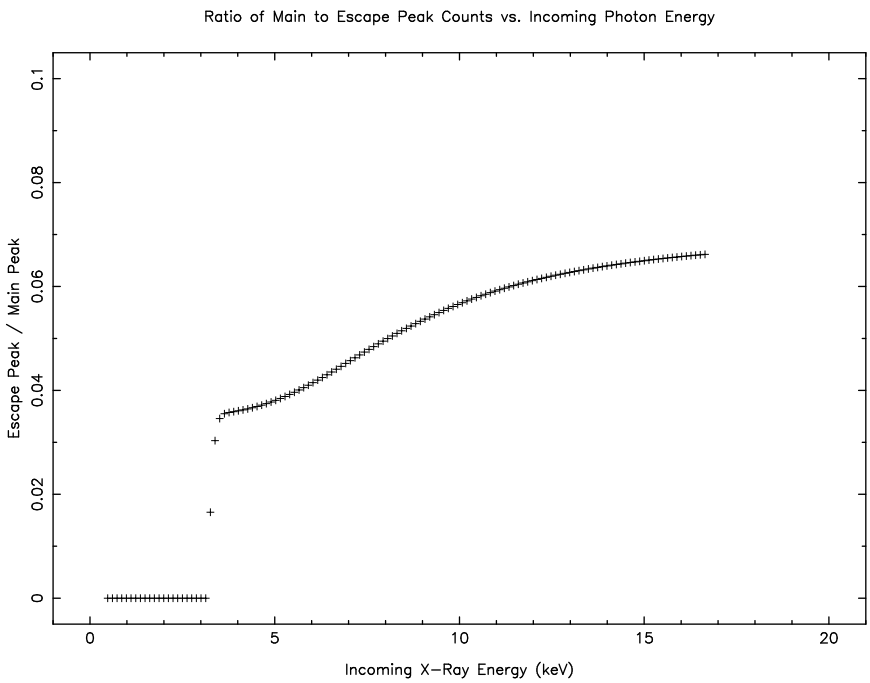

Fig. 37.— The ratio of the amplitudes of the main and escape peaks as a function of energy for the USA proportional counter chamber in the range 1-15 keV. There is no escape peak at energies below the Argon K-edge at 3.2029 keV. The escape peak height will have a variable amplitude ratio to the main peak over the USA energy range. The USA response matrices take this effect into account when their are produced.

7. Appendix: Space Charge Effects

The space charge in a gas filled proportional counter resulting from the slowly moving positive ions as they drift from the interaction location toward the cathode region is known to cause a significant change in the position and breadth of the energy peak created by monoenergetic X-rays (Hendricks 1969). This charge density causes a change in the electric field within the gas chamber to a value different from the field resulting from the applied voltage between the anode and the cathode under normal conditions.

The gas multiplication factor for a single cylindrical wire is given by

$$M = \exp\left[\frac{V\ln 2}{\Delta V ln(b/a)}\ln\left(\frac{V}{Kpa\ln(b/a)}\right)\right] \tag{25}$$

where

V	=	The applied voltage
ΔV	=	Potential difference which an electron moves between successive ionizing events
K	=	Minimum value E/p below which multiplication can not occur
p	=	P-10 gas pressure
a	=	Anode radius
b	=	Cathode radius

For P-10 gas $\Delta V = 23.6$ volts and $K = 4.8 \times 10^4$ volts cm^{-1} atm (Knoll 2000). The relative shift in multiplication space of a beam of monoenergetic X-ray photons is given by

$$\frac{\delta E}{E} = \frac{\delta M}{M} = -M(\frac{E}{W})(\frac{peb^2 R\ln 2}{4\Delta V L\mu V})\left[1+\ln\left(\frac{V}{Kpa\ln(b/a)}\right)\right] \tag{26}$$

where

R	=	Mean count rate
W	=	Mean energy required to create an ion-electron pair
L	=	Length of the anode wire
μ	=	Mobility of the ions in P-10 gas

For the parameters of USA the nominal multiplication factor is about 2270 and the relative shift in energy of the energy of the incident X-rays is only about 10^{-6} for count rates near 1 Crab. Thus, space charge effects are not important for the USA detectors even at their highest event rates.

8. Appendix: Orbital Dependence of the Gain

Given the clear difference in gain detected between the ascending and descending observations, and given that we know that USA is always in the dark in descending orbits and in the sun in ascending ones, it would seem plausible that the observed differences in the detector gain had something to do with temperature. In the absence of convection, a temperature gradient could be maintained between the two different layers of the chamber (which are nevertheless connected, and therefore would quickly reach a thermal equilibrium on the ground where convection is present). The question we ask ourselves, therefore, is how large a temperature gradient do we need to cause the observed 20% effect in gain?

We begin by writing down a first order differential equation which describes the dependence of the gain on the voltage and the density. A change in voltage implies a change in electric field strength (which is proportional to V) and therefore an increase in gas amplification. Conversely, an increase in pressure (or decrease in density) increases the mean free path, and, once again, increases the amplification in the gas. In the proportional region of the gas (where USA operates), we can write:

$$\frac{dG}{dV^*} = \alpha G \tag{27}$$

where we have defined:

$$V^* = \frac{V}{\rho} \tag{28}$$

and therefore:

$$dV^* = -\frac{V}{\rho^2}\, d\rho \tag{29}$$

Separating variables in equation 27 and integrating, we obtain:

$$\frac{dG}{G} = \alpha\, dV^* \tag{30}$$

$$\int \frac{dG}{G} = \ln G = \alpha V^* + C = \int \alpha\, dV^* \tag{31}$$

We use the fact that for P-10 (90% Ar, 10% CH_4) in the proportional region, a change in voltage of 100 V has the effect of doubling the gain:

$$2Ce^{\frac{\alpha V_0}{\rho}} = Ce^{\frac{\alpha(V_0+100)}{\rho}} \tag{32}$$

from which we deduce that:

$$\alpha = \rho\frac{\ln 2}{100} \tag{33}$$

Using equations 33 and 29 into 30 we obtain the following:

$$\frac{dG}{G} = -V\frac{\ln 2}{100}\frac{d\rho}{\rho} \tag{34}$$

From the ideal gas law, we have:

$$PV = NkT \tag{35}$$

$$\rho = \frac{N}{V} \tag{36}$$

$$T = \frac{P}{\rho k} \tag{37}$$

$$\frac{dT}{T} = -\frac{d\rho}{\rho} \tag{38}$$

Finally, plugging this into equation 34, we get:

$$\frac{dG}{G} = V\frac{\ln 2}{100}\frac{dT}{T} \tag{39}$$

$$\Delta T \approx \frac{100T}{V\ln 2}\frac{\Delta G}{G} \tag{40}$$

where $\frac{\Delta G}{G}$ is the observed change in gain of around 20% between the ascending and descending node observations, V is the chamber voltage, which is roughly held constant at around $2775V$ and T is the temperature of the chamber, which is around $285K$. Using all these numbers, we get:

$$\Delta T \approx \frac{(100)(285K)}{\ln 2(2775V)}(0.20) \approx 3K \tag{41}$$

The following plots show the temperatures of the back plate (UD1TBP) and that of the thermocouple located inside the chamber (USAST4) plotted together, for the times which span the calibration observations shown in Figures 20 and 21. The vertical line shows roughly where the calibration observation would fall. As can be seen, in the first observation we see a temperature gradient of around 2.5-3K, whereas in the second case there is basically no temperature gradient. Furthermore, it is clear from the several orbits displayed in Figure 38 that there is a clear temperature gradient whenever the satellite is on the ascending side of the orbit, whereas there is virtually no temperature gradient when we it is on the descending node (especially in the part of the orbit where USA would be observing, i.e. between the belts). The phase lag between the two temperature curves is consistent with the fact that the "back" takes longer to heat up, and therefore to cool down than the "front"

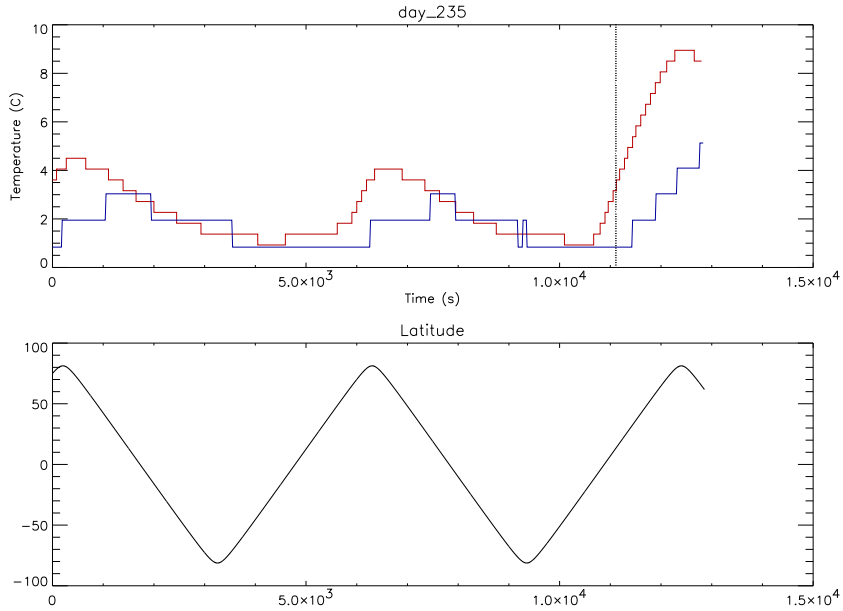

Fig. 38.— Day 235 (Ascending)

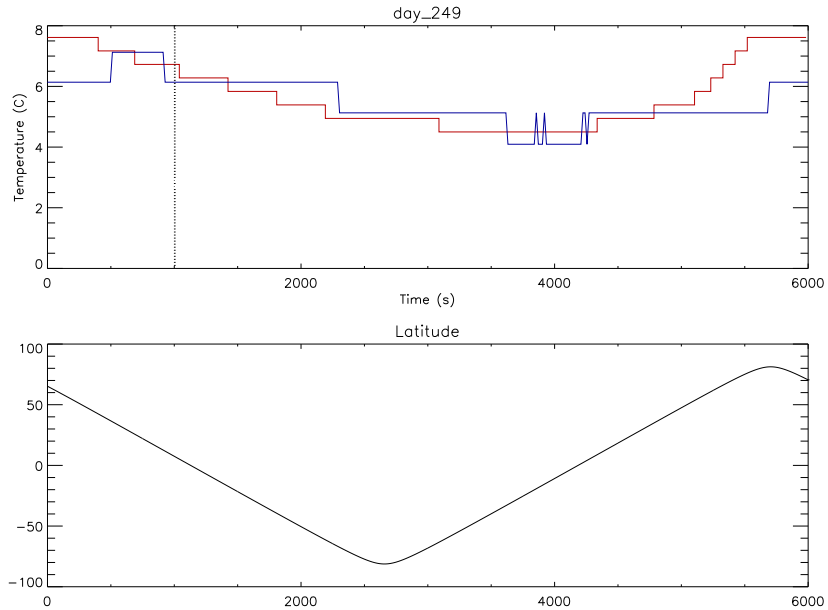

Fig. 39.— Day 249 (Descending)

9. Appendix: Energy-Channel Boundaries

Table 16 shows the energy boundaries for all PHA channels for the descending orbit segment observation of the Crab Pulsar on November 30, 1999. The spectral fit resulting from this observation is given in Tables 14 and 15 under ObsID Y1999 D334 055250. Channel 0 is artificially small in energy width because the energy-to-channel gain curve predicts negative energy boundary values for the first two channels. We artificially adjust these values to give positive numbers. Because the data in this channel is never used for any source analysis purpose this proceedure is acceptable.

Table 16. **USA Descending Node Energy-Channel Boundaries**

Raw PHA (channel)	E_{min} (keV)	E_{center} (keV)	E_{max} (keV)	ΔE (keV)	DIB Mode 1&2 (channel)	DIB Mode 3&4 (channel)	DIB Mode 5 (channel)
0	0.000100	0.007654	0.015208	0.015108	0	0	0
1	0.015208	0.082673	0.150138	0.134930	0	0	0
2	0.150138	0.217570	0.285002	0.134865	0	0	1
3	0.285002	0.352402	0.419803	0.134800	0	0	1
4	0.419803	0.487170	0.554538	0.134735	0	0	2
5	0.554538	0.621873	0.689209	0.134671	0	0	2
6	0.689209	0.756512	0.823815	0.134606	0	0	3
7	0.823815	0.891086	0.958357	0.134542	0	0	3
8	0.958357	1.025596	1.092834	0.134477	1	0	4
9	1.092834	1.160041	1.227247	0.134413	1	0	4
10	1.227247	1.294421	1.361596	0.134349	1	0	5
11	1.361596	1.428738	1.495880	0.134284	1	0	5
12	1.495880	1.562990	1.630100	0.134220	1	0	6
13	1.630100	1.697178	1.764256	0.134156	1	0	6
14	1.764256	1.831301	1.898347	0.134092	1	0	7
15	1.898347	1.965361	2.032374	0.134027	1	0	7
16	2.032374	2.099356	2.166338	0.133963	2	1	8
17	2.166338	2.233287	2.300237	0.133899	2	1	8
18	2.300237	2.367155	2.434072	0.133835	2	1	9
19	2.434072	2.500958	2.567844	0.133771	2	1	9
20	2.567844	2.634697	2.701551	0.133707	2	1	10
21	2.701551	2.768373	2.835195	0.133644	2	1	10
22	2.835195	2.901984	2.968774	0.133580	2	1	11
23	2.968774	3.035532	3.102290	0.133516	2	1	11
24	3.102290	3.180903	3.259516	0.157226	3	1	12
25	3.259516	3.327040	3.394565	0.135049	3	1	12
26	3.394565	3.462085	3.529604	0.135039	3	1	13
27	3.529604	3.597118	3.664633	0.135029	3	1	13
28	3.664633	3.732142	3.799651	0.135018	3	1	14
29	3.799651	3.867155	3.934659	0.135008	3	1	14
30	3.934659	4.002158	4.069657	0.134998	3	1	15
31	4.069657	4.137151	4.204644	0.134988	3	1	15
32	4.204644	4.272133	4.339622	0.134977	4	2	16
33	4.339622	4.407105	4.474589	0.134967	4	2	16
34	4.474589	4.542067	4.609545	0.134957	4	2	17
35	4.609545	4.677019	4.744492	0.134946	4	2	17
36	4.744492	4.811960	4.879428	0.134936	4	2	18
37	4.879428	4.946891	5.014354	0.134926	4	2	18
38	5.014354	5.081812	5.149269	0.134916	4	2	19
39	5.149269	5.216722	5.284175	0.134905	4	2	19
40	5.284175	5.351622	5.419070	0.134895	5	2	20
41	5.419070	5.486512	5.553954	0.134885	5	2	20
42	5.553954	5.621392	5.688829	0.134875	5	2	21
43	5.688829	5.756261	5.823693	0.134864	5	2	21
44	5.823693	5.891120	5.958547	0.134854	5	2	22
45	5.958547	6.025969	6.093391	0.134844	5	2	22
46	6.093391	6.160808	6.228224	0.134833	5	2	23
47	6.228224	6.295636	6.363048	0.134823	5	2	23
48	6.363048	6.430454	6.497861	0.134813	6	3	24
49	6.497861	6.565262	6.632663	0.134803	6	3	24
50	6.632663	6.700059	6.767456	0.134792	6	3	25
51	6.767456	6.834847	6.902238	0.134782	6	3	25
52	6.902238	6.969624	7.037010	0.134772	6	3	26
53	7.037010	7.104391	7.171771	0.134762	6	3	26
54	7.171771	7.239147	7.306523	0.134751	6	3	27
55	7.306523	7.373893	7.441264	0.134741	6	3	27
56	7.441264	7.508629	7.575995	0.134731	7	3	28
57	7.575995	7.643355	7.710716	0.134721	7	3	28

Table 16—Continued

Raw PHA (channel)	E_{min} (keV)	E_{center} (keV)	E_{max} (keV)	ΔE (keV)	DIB Mode 1&2 (channel)	DIB Mode 3&4 (channel)	DIB Mode 5 (channel)
58	7.710716	7.778071	7.845426	0.134710	7	3	29
59	7.845426	7.912776	7.980126	0.134700	7	3	29
60	7.980126	8.047471	8.114816	0.134690	7	3	30
61	8.114816	8.182156	8.249496	0.134680	7	3	30
62	8.249496	8.316830	8.384165	0.134669	7	3	30
63	8.384165	8.451495	8.518824	0.134659	7	3	30
64	8.518824	8.586149	8.653473	0.134649	8	4	31
65	8.653473	8.720793	8.788112	0.134639	8	4	31
66	8.788112	8.855426	8.922741	0.134628	8	4	31
67	8.922741	8.990050	9.057359	0.134618	8	4	31
68	9.057359	9.124663	9.191967	0.134608	8	4	32
69	9.191967	9.259266	9.326564	0.134598	8	4	32
70	9.326564	9.393858	9.461152	0.134588	8	4	32
71	9.461152	9.528441	9.595729	0.134577	8	4	32
72	9.595729	9.663013	9.730296	0.134567	9	4	33
73	9.730296	9.797575	9.864853	0.134557	9	4	33
74	9.864853	9.932127	9.999400	0.134547	9	4	33
75	9.999400	10.066668	10.133936	0.134536	9	4	33
76	10.133936	10.201199	10.268462	0.134526	9	4	34
77	10.268462	10.335720	10.402978	0.134516	9	4	34
78	10.402978	10.470231	10.537484	0.134506	9	4	34
79	10.537484	10.604732	10.671979	0.134495	9	4	34
80	10.671979	10.739222	10.806465	0.134485	10	5	35
81	10.806465	10.873702	10.940940	0.134475	10	5	35
82	10.940940	11.008172	11.075405	0.134465	10	5	35
83	11.075405	11.142632	11.209859	0.134455	10	5	35
84	11.209859	11.277081	11.344304	0.134444	10	5	36
85	11.344304	11.411521	11.478738	0.134434	10	5	36
86	11.478738	11.545950	11.613162	0.134424	10	5	36
87	11.613162	11.680368	11.747575	0.134414	10	5	36
88	11.747575	11.814777	11.881979	0.134404	11	5	37
89	11.881979	11.949176	12.016372	0.134393	11	5	37
90	12.016372	12.083564	12.150755	0.134383	11	5	37
91	12.150755	12.217942	12.285128	0.134373	11	5	37
92	12.285128	12.352309	12.419491	0.134363	11	5	38
93	12.419491	12.486667	12.553843	0.134352	11	5	38
94	12.553843	12.621014	12.688186	0.134342	11	5	38
95	12.688186	12.755352	12.822518	0.134332	11	5	38
96	12.822518	12.889679	12.956839	0.134322	12	6	39
97	12.956839	13.023995	13.091151	0.134312	12	6	39
98	13.091151	13.158302	13.225453	0.134301	12	6	39
99	13.225453	13.292598	13.359744	0.134291	12	6	39
100	13.359744	13.426884	13.494025	0.1342814	12	6	40
101	13.494025	13.561160	13.628296	0.1342711	12	6	40
102	13.628296	13.695426	13.762556	0.1342618	12	6	40
103	13.762556	13.829682	13.896807	0.1342506	12	6	40
104	13.896807	13.963927	14.031047	0.1342404	13	6	41
105	14.031047	14.098162	14.165277	0.134230	13	6	41
106	14.165277	14.232387	14.299497	0.134220	13	6	41
107	14.299497	14.366602	14.433707	0.134210	13	6	41
108	14.433707	14.500807	14.567906	0.134200	13	6	42
109	14.567906	14.635001	14.702096	0.134189	13	6	42
110	14.702096	14.769185	14.836275	0.134179	13	6	42
111	14.836275	14.903359	14.970444	0.134169	13	6	42
112	14.970444	15.037523	15.104602	0.134159	14	7	43
113	15.104602	15.171677	15.238751	0.134149	14	7	43
114	15.238751	15.305820	15.372889	0.134138	14	7	43
115	15.372889	15.439953	15.507018	0.134128	14	7	43

Table 16—Continued

Raw PHA (channel)	E_{min} (keV)	E_{center} (keV)	E_{max} (keV)	ΔE (keV)	DIB Mode 1&2 (channel)	DIB Mode 3&4 (channel)	DIB Mode 5 (channel)
116	15.507018	15.574077	15.641136	0.134118	14	7	44
117	15.641136	15.708190	15.775243	0.134108	14	7	44
118	15.775243	15.842292	15.909341	0.134098	14	7	44
119	15.909341	15.976385	16.043429	0.134087	14	7	44
120	16.043429	16.110467	16.177506	0.134077	15	7	45
121	16.177506	16.244539	16.311573	0.134067	15	7	45
122	16.311573	16.378602	16.445630	0.134057	15	7	45
123	16.445630	16.512653	16.579677	0.134047	15	7	45
124	16.579677	16.646695	16.713713	0.134037	15	7	46
125	16.713713	16.780727	16.847740	0.134026	15	7	46
126	16.847740	16.914748	16.981756	0.134016	15	7	46
127	16.981756	17.048759	17.115762	0.134006	15	7	46
128	17.115762	17.182760	17.249758	0.133996	16	8	47

10. Appendix: Codes

To Be Added Later as report is finalized.

REFERENCES

Arnaud, K. A., George, I. M., & Tennant, A. F. 1992, The OGIP Spectral File Format, Legacy: The Journal of the HEASARC/NASA-GSFC, no.2, p.65

Bambynek, W., Crasemann, B., Fink, R. W., Freund, H., Mark, H., Swift, C. D., Price, R. E., & Venugopala Rao, P. 1972, Reviews of Modern Physics, 44, 716

Browne, E. and Firestone, R. B. 1986, Table of Radioactive Isotopes (New York: John Wiley & Sons)

Fink, H. H., Schmitt, J. H. M. M., & Harnden, F. R. 1988, A&A, 193, 345

George, I. M., Arnaud, K. A., Price, B., & Ruamsuwan, L. 1992, The Calibration Requirements for Spectral Analysis, Legacy: The Journal of the HEASARC/NASA-GSFC, no.2, p.51

Hendricks, R. W. 1969, Rev. Sci. Instrum., 40, 1216

Inoue, H., Koyama, K., Matsuoka, M., Ohashi, T., & Tanaka, Y. 1978, Nucl. Instrum. & Meth., 157, 295

Jahoda, K., Markwardt, C. B., Rots, A. H., Stark, M. J., Swank, J. H., Strohmayer, T. E., & Zhang, W. 2003, Draft Report

Jahoda, K. & McCammon, D. 1988, Nucl. Instrum. & Meth. A, 272, 800

Knoll, G. 2000, Radiation Detection and Measurement (New York: John Wiley & Sons)

Kowalski, M. P., Cruddace, R. G., Snyder, W. A., Fritz, G. G., Ulmer, M. P., & Fenimore, E. E. 1993, ApJ, 412, 489

Monteiro, C. M. B., Simoes, P. C. P. S., Veloso, J. F. C. A., Santos, J. M. F., & Conde, C. A. N. 2003, Nucl. Instrum. & Meth. A, 505, 233

Ray, P. S., Wood, K. S., Fritz, G., Hertz, P., Kowalski, M., Johnson, W. N., Lovellette, M. N., Wolff, M. T., Yentis, D., Bandyopadhyay, R. M., Bloom, E. D., Giebels, B., Godfrey, G., Reilly, K., Saz Parkinson, P., Shabad, G., Michelson, P., Roberts, M., Leahy, D. A., Cominsky, L., Scargle, J., Beall, J., Chakrabarty, D., & Kim, Y. 2001, in AIP Conference Proceedings, Vol. 599, X-ray Astronomy 1999 – Stellar Endpoints, AGN, and the Diffuse Background, ed. G. Malaguti, G. Palumbo, & N. White (Melville, New York: AIP), 336

Sauli, F. 1977, CERN 77-09

Shabad, G. 2000, PhD thesis, Stanford Universtiy

Snowden, S. L. & Freyberg, M. J. 1993, ApJ, 404, 403

Toor, A. & Seward, F. D. 1974, Astron. J., 79, 995

Wen, H. C. 1997, PhD thesis, Stanford Universtiy

Willingale, R., Aschenbach, B., Griffiths, R. G., Sembay, S., Warwick, R. S., Becker, W., Abbey, A. F., & Bonnet-Bidaud, J.-M. 2001, A&A, 365, L212

This preprint was prepared with the AAS LaTeX macros v5.0.